Collisional Dissociation of CO: ab initio Potential Energy Surfaces and Quasiclassical Trajectory Rate Coefficients

David W. Schwenke,[*] Richard L. Jaffe[†] and Galina M. Chaban[‡]

NASA Ames Research Center
Mail Stop 258-2, P.O. Box 1
Moffett Field, CA 94035-0001

April 6, 2016

Abstract

We have generated accurate global potential energy surfaces for CO+Ar and CO+O that correlate with atom-diatom pairs in their ground electronic states based on extensive *ab initio* electronic structure calculations and used these potentials in quasi-classical trajectory nuclear dynamics calculations to predict the thermal dissociation rate coefficients over 5000-35000 K. Our results are not consistent with the interpretation of the 20-45 year old experimental results. For CO + Ar we obtain fairly good agreement with the experimental rate coefficients of Appleton *et al.* (1970) and Mick and Roth (1993), but our computed rate coefficients exhibit a stronger temperature dependence. For CO + O our dissociation rate coefficient is in close agreement with the value from the Park model, which is an empirical adjustment of older experimental results. However, we find the rate coefficient for CO + O is only 1.5 to 3.3 times larger than CO + Ar over the temperature range of the shock tube experiments (8000-15,000 K). The previously accepted value for this rate coefficient ratio is 15, independent of temperature. We also computed the rate coefficient for the CO + O exchange reaction which forms C + O_2. We find this reaction is much faster than previously believed and is the dominant process in the removal of CO at temperatures up to 16,000 K. As a result, the dissociation of CO is accomplished in two steps (react to form C+O_2 and then O_2 dissociates) that are endothermic by 6.1 and 5.1 eV, instead of one step that requires 11.2 eV to break the CO bond.

Our recommended dissociation rate coefficients in units of cm^3 molecule^{-1} s^{-1} over the temperature range $7500 - 20,000$K are: CO + Ar $\rightarrow$ C + O + Ar $k_{diss} = 2.781 \times 10^{-5} T^{-0.85} \exp(-128741/T)$ CO + O $\rightarrow$ C + O + O

[*]E-mail: david.w.schwenke@nasa.gov
[†]E-mail: richard.l.jaffe@nasa.gov
[‡]E-mail:galina.m.chaban@nasa.gov

$k_{diss} = 1.733 \times 10^{-1} T^{-1.71} \exp(-128741/T)$, and our recommended rate coefficient for the exchange reaction over the temperature range 5000-20,000 K is: $CO + O \rightarrow C + O_2$ $k_{exch} = 5 \times 10^{-10} \exp(-77600/T)$.

1 Introduction

Spacecraft entering the atmosphere of a planet at hypersonic speeds experience extreme heating due to thermal and chemical non-equilibrium effects in the bow shock layer, which forms ahead of the vehicle. Mars has an atmosphere that is 96% CO_2 with 1.9% N_2 and 1.9% Ar by volume and other minor constituents, [1] but the pressure at the surface is only 0.008 bar[2]. For typical Mars entries with 1-3 m diameter objects, the spacecraft velocity is 5-8 km/s and the temperature in the shock layer can reach 10,000 K. Under these conditions, CO_2 rapidly dissociates and the dominant species in the shock layer are CO and O. Behind the shock, the gas is no longer in thermal equilibrium and the translational energy mode is highly excited compared to internal energy modes. This results in a radiative heat flux from the bow shock layer that forms circa 20 cm in front of the spacecraft. Computational models have been developed to predict the magnitude of non-equilibrium heating for the Mars entry vehicles. The model widely used for engineering studies of spacecraft entering the Martian atmosphere was developed by Park more than 20 years ago[3], based on a series of papers published in the late 1980's[4],[5],[6],[7]. That model uses two temperatures - translational (T) and vibrational (T_v) - to describe the non-equilibrium condition. The Landau-Teller[8][9] expression is used to compute T_v and the rotational mode is assumed to be in equilibrium with translation at temperature T. The extent of electronic excitation is governed by T_v. In addition, dissociation rate coefficients are expressed in terms of an average temperature $T_{av} = \sqrt{TT_v}$.

For these Mars entry conditions, most of the radiative heat flux is due to emission from the CO 4th positive system.[10] Thus, an important reaction rate for modeling the heating of a spacecraft entering the atmosphere of Mars is the dissociation of ground state CO due to heavy particle impact. The primary collision partners involved in the dissociation of CO are CO and O, but the best experimental CO dissociation rate coefficient data at the time that Park developed his model was for CO+Ar collisions. Rate coefficients for other collision partners were expressed relative to the CO+Ar values by a constant multiplicative scaling factor. For example, the efficiency of O, N and C atoms in promoting dissociation was considered to be 15 times the argon rate coefficient and for CO+CO the factor was taken to be 10[3].

The proposed rate coefficients for collisional dissociation of CO by collision with argon and oxygen atoms are generally in fair agreement with the published shock tube experiments, all of which date to before 1993. However, these measurements yielded results in a fairly narrow temperature range, so how extrapolation is done is a significant concern. The experiments using CO/Ar mixtures were carried out by Davies[11], Appleton *et al.*[12](who also used CO+O$_2$+Ar)

and Mick et al.[13] Determinations for pure CO were carried out by Presley et al.,[14] Chackarian[15] and Hanson.[16] All the data up to 1974 are tabulated and compared in the compendium by Baulch *et al.*[17] who included their recommended Arrhenius rate coefficient expression, which is mostly based on the work of Davies and Appleton *et al.* That compendium also tabulated relative dissociation efficiencies for different CO collision partners relative to CO + Ar, *e.g.*, rate coefficient ratios $k_{diss}^{CO+CO}/k_{diss}^{CO+Ar} = 1 - 2$ and $k_{diss}^{CO+O}/k_{diss}^{CO+Ar} = 15$. Note the Baulch compendium and the Park model give values for the efficiency of CO that differ by an order of magnitude.

Unfortunately, the measurements do not cover a very wide temperature and also do not cover the temperatures of interest for the higher entry speeds (>12000K). Thus extrapolation to the desired temperature range is strongly dependent on the functional form used to interpolate the measurements. Another problem is the dispersion of the experimental results using different techniques at different laboratories. In addition, more recent measurements of the radiative flux produced by high-speed flows of $CO_2 + N_2$ mixtures has demonstrated that the original Park model over predicts the amount of CO 4th positive radiation present in the shock layer[18]. In that work, Johnston and Brandis found that increasing the CO dissociation rate coefficient by a factor of 5 led to better agreement between model calculations and experiment.

Thus, we have studied the title reactions using first principles. Our goal is two fold: to accurately assess the temperature dependence of these reactions, bridging the temperature range of the experimental measurements to that required for the entry simulations, and secondly, to try and assess which experiment gives rise to the most reliable results.

Our strategy[19] is as follows: for each reaction we first carry out extensive *ab initio* electronic structure calculations of the potential energy surface (PES) on a grid of geometries and then form an analytic representation of the computed data that can be used to interpolate and extrapolate to all geometries, then we use the quasi-classical trajectory method (with these PESs) to compute the thermal equilibrium dissociation rates for the temperature range of interest.

2 *ab initio* Calculations for CO+Ar

Our initial strategy was the same as we have used before for the $N_2 + N_2$ system,[20][19] namely to carry out a large number of calculations using the coupled cluster singles and doubles (CCSD) method with perturbative triples, denoted CCSD(T), with the CO bond length restricted to values where the CCSD(T) method gives good results, and then augment these results with the more expensive ACPF calculations for longer CO bond lengths up to 10 a_o, where one a_o is the Bohr radius. These calculations were carried out using the MOLPRO program.[21] Because we want to obtain accurate energies all the way out to dissociation, we need a one-particle basis set that has sufficient diffuse functions. We chose to use the aug-cc-pVQZ basis[22] on all atoms. All calculations were carried out using C_s symmetry, with the orbitals transforming as A' or A''. Since the

ground electronic state of CO transforms as $^1\Sigma^+$ and the ground electronic state of Ar transforms as ^1S, the electronic state of interest for CO+Ar has symmetry $^1A'$.

The CCSD(T) calculations progressed without incident, but the ACPF calculations were problematic. The issues became readily apparent when we tried to simultaneously fit the CCSD(T) and ACPF data: decent fits for the CCSD(T) data were obtained, but the ACPF data appeared to be very noisy. We tried numerous techniques to filter out erroneous data, such as looking at the weight of the reference function in the ACPF results, but nothing worked satisfactorily.

In these ACPF calculations, we determined the orbitals by multi-configuration Hartree-Fock (MCHF) calculations for the lowest A' state, doubly occupying the six a' and single a'' orbitals corresponding to the C and O $1s$ like orbitals and Ar $1s$, $2s$, $2p$ like orbitals, and in our active space we included nine a' and three a'' orbitals, corresponding to the C and O $2s$, $2p$ and Ar $3p$ like orbitals. Upon analyzing the ACPF results it became apparent that there were two problems. The first problem was evident from ACPF calculations on just the CO molecule. These calculations are carried out using C_{2v} symmetry. At large bond lengths, the first excited $^1\Sigma^+$ state comes down in energy and becomes degenerate with the ground state. However the ACPF method is only valid when the state of interest is non-degenerate. We found that in the asymptotic region, the ACPF calculation, and perhaps also the MCHF calculation, would converge on the first excited $^1\Sigma^+$ state rather than the desired state. This incorrect convergence caused random discontinuous jumps in the computed energies. When Ar is added and the symmetry is lowered to C_s, the situation becomes even worse: then in the asymptotic region, the lowest $^1A'$ state becomes five-fold degenerate.

The second problem concerns the O $2s$ like orbital and the Ar valence orbitals. As CO dissociates, the optimum solution for ^3P O has the $2s$ orbital doubly occupied, and when Ar is not strongly interacting with CO, the optimum solution for the Ar orbitals is also doubly occupied orbitals. When the optimum solution for an orbital in the active space leads to an occupation number sufficiently close to 2, the MCHF energy is invariant to rotations between that orbital and the orbitals that were restricted to be doubly occupied. Since in these ACPF calculations, we only correlate the active orbitals, slight amounts of doubly occupied orbitals that mix with a' orbitals in the active space leads to random unphysical additional correlation energy. When these orbitals are the Ar $1s$ like orbital, a very small amount of mixing gives significant additional energy because the correlation energy of the Ar $1s$ orbital is so very large.

Thus we carried out multi-reference configuration interaction (MRCI) calculations using different molecular orbitals. The MRCI method works well even when there are degenerate electronic states, but is not quite as accurate as the ACPF method, for only the latter includes corrections for quadruple excitations. In the new MCHF calculations, we doubly occupied ten a' and two a'' orbitals: the extra four a' orbitals and extra a'' orbital correspond to the O $2s$ like orbital and the Ar $3s$ and $3p$ like orbitals. Then there are five a' and two a'' orbitals in the active space corresponding to the C $2s$ and $2p$ and O $2p$ like orbitals. In these calculations, we minimized energy of the lowest 5 $^1A'$ states,

with the weight factors computed with the dynamic weights of Deskevich *et al.*[23] with energy parameter 2 eV^{-1}. We then determined energies using the MRCI method keeping the lowest six a' and lowest a'' orbitals doubly occupied in all configurations and the next four a' and next a'' orbitals doubly occupied in all reference configurations. We computed five roots using the projected state method,[21] but ended up only using the first root (which was sufficiently separated from the higher roots) and using the MRCI+Q energy, where the +Q denotes the addition of the Davison quadrupoles correction. Using the +Q gave better consistency with the CCSD(T) energies than the MRCI energy.

We computed 827 MRCI+Q energies and 2243 CCSD(T) energies. The geometries were chosen using approximate Jacobi coordinates for Ar+CO: r_{vib} is the CO bond length, R_c is the distance from Ar to the CO bond midpoint, and θ_c is the Ar-CO bond midpont-C angle.The MRCI+Q calculations were for r_{vib}=2.2-10 a_o, θ_c=0,22,45,90,135,157,180°, and R_c=2.0-20 a_o, while the CCSD(T) energies were for r_{vib}=1.6-3.0 a_o, θ_c=0-180 in steps of 15°, and R_c=3.5-20 a_o.

3   *ab initio* Calculations for CO+O

The three potential energy surfaces of CO+O that correlate to the ground state of CO, $^1\Sigma^+$ and the ground state of oxygen atom, ^3P, are the lowest $^3A'$ surface and the lowest two $^3A''$ surfaces. Thus we need to consider three PESs for this process. Here we have the great advantage that *ab initio* data for these surfaces is already available from Schmidt *et al.*[24] Those calculations used the aug-cc-pVQZ basis like we did for CO+Ar, and computed three roots in $^3A'$ and $^3A''$ symmetry using the MRCI method. However, since that study was focused on photodissociation dynamics rather than collision dynamics, Schmidt *et al.* did not cover all the geometries that we require for the present work. Their calculations were carried out on an evenly spaced direct product grid of the two CO bond lengths and the cosine of the OCO bond angle. Thus we carried out additional calculations using the same strategy as described above: we carried out MRCI+Q and CCSD(T) calculations using the aug-cc-pVQZ basis and analogous active space as described above. In the O+C+O limit, there are 27 degenerate triplet states, with 14 transforming as A' and 13 as A'', and in our MCHF calculations, we averaged over all 27 states, with dynamic weights as described above. The aug-cc-pVQZ basis CCSD(T) calculations used RHF orbitals and the RCCSD(T) method as programed in MOLPRO. Separate calculations were carried out for the lowest $^3A'$ state and the lowest $^3A''$ state. We also carried out some aug-cc-pVTZ CCSD(T) calculations using Gaussian09:[25] these calculations used UHF orbitals and the UCCSD(T) method and did not take advantage of symmetry, thus only yielded results for the A' surface. In our MRCI+Q and QZ CCSD(T) calculations, we used the second order Douglas-Kroll-Hess method[26][27] to include scalar relativistic effects. Scalar relativistic effects were not included in the calculations of Schmidt *et al.*[24] nor in our TZ CCSD(T) calculations.

We also have to be very careful when using the Schmidt data because their MCHF calculations included the O 2s-like orbitals in the active space and state averaged only over the lowest three states of $^3A'$ or $^3A''$ symmetry with equal weights. Recall that including the O $2s$ like orbitals in the active space caused problems for CO+Ar, and the problem with averaging over three roots with equal weights is that when the three states are widely separated in energy, the number of local minima in orbital rotation space increases. There is greater possibility that one of these is found instead of the global minimum. The use of dynamic weights[23] largely avoids this difficulty. Furthermore in the Schmidt *et al.* MRCI calculations, three roots were computed using the combined contracted $N-2$ functions formed from the three lowest roots of the active space. In our experience, this means that if the highest root changes character at some geometry, which is not at all unlikely, then using the combined contracted $N-2$ functions[28] leads to discontinuous jumps in the energies of all roots. In our calculations, we use the projected state method whereby each root uses the contracted $N-2$ functions appropriate for the zero order description of that particular root.

For these reasons, our MRCI+Q calculations are more reliable than those from Schmidt *et al.*, and also *much* less costly.

4 Analytic Representation of CO+Ar

We separated the electronic energies into two parts: V^{CO}, the diatomic potential energy, and V^{int}, the rest. For the CCSD(T) and MRCI+Q data, we determined V^{CO} from CO+Ar calculations with the largest Ar to center of CO distance: this was typically 20 a_o. Then we fit V^{int} assuming that we could mix the CCSD(T) and MRCI+Q data freely apart from a single multiplicative factor: this factor was optimized in the fitting process, and the final result was to multiply the CCSD(T) V^{int} values by 1.022.

The final functional form we used was[29][30]

$$V^{int} = F(r_{vib}, R_c, \theta_c)[V^{\mathrm{ArC}}(R_{\mathrm{ArC}}) + V^{\mathrm{ArO}}(R_{\mathrm{ArO}})] + V^{LR}(R_{\mathrm{ArC}}, R_{\mathrm{ArO}}), \quad (1)$$

with r_{vib} the distance between the C and O atoms, R_c the distance from the Ar atom to the CO bond midpoint, and θ_c the angle between the CO bond and the vector from the CO bond midpoint to the Ar atom: $\theta_c = 0$ corresponds to linear ArCO, R_{ArX} the distance between the Ar atom and atom X, with X being C or O, F is a modulating/damping function,

$$V^{\mathrm{ArX}}(R) = 18Z_{\mathrm{X}} \exp(-\alpha^{\mathrm{ArX}}R)/R, \quad (2)$$

Z_{X} the atomic number of atom X, and

$$V^{LR} = -C_6^{\mathrm{ArC}}/(R_{\mathrm{ArC}}^6 + \delta^6) - C_6^{\mathrm{ArO}}/(R_{\mathrm{ArO}}^6 + \delta^6). \quad (3)$$

We initially represented F as

$$F = 1 + \exp\left[-d\,(r_{vib} - r_c)^p\right]\left\{\exp[-g(R_c - R_1)^2]\sum_{ij} C_{ij}^{(1)} r_{vib}^i \cos^j(\theta_c)\right.$$

$$\left. + \exp[-g(R_c - R_2)^2]\sum_{ij} C_{ij}^{(2)} r_{vib}^i \cos^j(\theta_c)\right\} \quad (4)$$

with $r_c = 2\,a_o$ and $p = 2$, but found that sometimes in the extrapolation region of no physical interest, $i.e.$ when one of the R_{ArX} distances is very small, F would become negative, and since one of the V^{ArX} would be become extremely large and positive in this region, spurious holes would occur in V^{int}. These holes would also render the PES unfit for use in quantum scattering calculations. Thus we modified this expression so that

$$F = 1 + \mathcal{F}\mathcal{D}(\mathcal{F}), \quad (5)$$

with $\mathcal{F} + 1$ given by the right hand side of Eq. 4, and

$$\mathcal{D}(X) = 1/[1 + \exp(-vX)]. \quad (6)$$

The parameter R_2 was given by $R_2 - R_1 = \sqrt{(-2O_g/g)}$ with δ and O_g fixed,[31] while the remaining parameters in Eqs. 3 and 4 were all optimized by weighted nonlinear least squares. The weights were set to $1/\max(V^{int}, \epsilon)$, with V^{int} the data being fitted and $\epsilon = 0.01$ E_h. The value of O_g, the overlap of the adjacent gaussians, was taken to be 0.95 and δ was taken to be 5 a_o. The parameter v in Eq. 6 was crudely optimized by trial and error. Good initial guesses for the non-linear parameters were obtained by sequentially fitting data most sensitive to particular parameters, $e.g.$ the long range parameters C_6^{ArC} and C_6^{ArO} were determined by a linear least squares to V^{int} weighted by $R_{\mathrm{ArC}}^3 R_{\mathrm{ArO}}^3$, then $\alpha = \alpha^{\mathrm{ArC}} = \alpha^{\mathrm{ArO}}$ was optimized by fitting to V^{int}, then α^{ArC} and α^{ArO} were independently optimized by fitting to V^{int}, and finally initial guesses for the coefficients $C_{ij}^{(n)}$ were determined by linear least squares with the rest of the parameters fixed. We then performed a non-linear fit with $\mathcal{D}$ set to unity, and finally we added in the parameter v in $\mathcal{D}$ and re-optimized all parameters. We settled on including all terms in Eq. 4 with $0 \leq i + j \leq 6$.

We iterated the optimization of all the parameters. After each optimization was complete, we computed the percentiles of the distribution of the weighted fitting errors. If a point had an error that was more negative than 5 times the tenth percentile or more positive than 5 times the ninetieth percentile, the weight for that point was made very small. Once this had been done for all the points with largest errors, we went back and performed a new fit, and checked the percentiles again. We repeated this until no additional points were eliminated. Out of the 3070 total points, 57 were eliminated.

This is an attempt at robust estimation whereby the influence of widely deviating points is diminished while maintaining standard non-linear least squares formulation - see $e.g.$ Press $et\ al.$[32].

Because the points were unequally weighted, it is hard to quantify the fitting error with a single number, but one measure of the fitting error is the average weighted error, and for this quantity we obtained 0.014. Recall that the weights are taken to be equal to $1/\max(V^{int}, \epsilon)$. Thus 0.014 means, for example, that geometries with energies less than ϵ will have typical errors of $0.014\epsilon = 0.00014$ $E_h = 0.088$ kcal/mol, while geometries with energies higher will have percent errors of a hundred times more, *i.e.* 1.4 percent. Thus this is a very satisfactory fit.

In Fig. 1, we show a typical cut through V^{int} for fixed R_c and θ_c, and one can see from this figure that the CCSD(T) and MRCI+Q results are quite consistent and the fit does a good job of interpolating the *ab initio* data, especially in the region near the equilibrium CO bond length of about 2.2 a_o. This region is expected to be crucial in the initial vibrational excitation.

In Figs. 2 to 4 we show contour maps of V^{int} for fixed r_{vib}. We also show for reference the geometries of the MRCI+Q and CCSD(T) points used to generate the analytic representation. For bond lengths near the CO equilibrium geometry, *i.e.* Fig. 2, the contours are rather featureless, with the expected weak van der Vaals minimum and repulsive walls. For a given repulsive energy, the Ar can get closer to the C atom than the O atom. As the C and O atoms pull apart, we see that, as a result of the electron density pulling away from the center of the diatomic (*i.e.* Fig. 3 to 4), the Ar can now approach closer to the center of the diatomic than to either of the atom.

In *e.g.* Fig. 3, we see some rather odd looking high energy contours, but these occur at sufficiently high energy to not be a concern: the highest energy contour is at 1 E_h.

5   Analytic Representation of CO+O

The potential surfaces of CO+O are much more complicated than that of CO+Ar. Compared to Ar, which has symmetry ^1S, the ground state of O has symmetry ^3P. In C_s symmetry, this means we have to consider electronic states of $^3A'$ and $^3A''$ symmetry. Furthermore, O can react with CO and the oxygen atoms can be exchanged (homogeneous exchange), and O can react with CO to form O_2+C. Also, there is an energy minimum on each PES corresponding to non-linear triplet states of CO_2. The functional form used for the CO+Ar PES is not suited to describe this situation. However we would still like to use some ideas that were valuable for CO+Ar. Thus we start by representing the potentials as the lowest eigenvalue of a matrix, with the diagonal elements a function like the one used for the CO+Ar PES. Initially we started with a two by two matrix corresponding to the CO+O' and CO'+O channels, but found there was an important deficiency in the vicinity of the global minimum of the ground state potentials. Thus we added a third diabatic state to describe that region, which improved things greatly, but the resulting analytic representation was still not sufficiently accurate. After inspecting numerous contour plots, we deduced that the global minimum diabat was also being forced to represent the

O_2+C channel, even though the number of *ab initio* data points in this region was rather small. Thus we added a fourth diabat to describe that channel, and then we obtained satisfactory analytic representations.

Now we performed a separate fit for the two $^3A''$ surfaces. In principle if our fitting model was reliable, then the two $^3A''$ surfaces would come out as eigenvalues of the same matrix. But at minimum, in order to represent the CO+O and O_2+C asymptotic degeneracies, the matrix would need to be at least 7×7. Furthermore, in some strongly interacting regions, there are avoided crossings with multiple other roots, and describing this accurately would required even more diabatic states. For these reasons and the fact that we do not see strong interaction between the lowest two $^3A''$ surfaces, we fit the surfaces separately.

There are three other consequences of representing the data in terms of the eigenvalues of a matrix. The first two result from not being able to subtract off the diatomic potential. First we cannot simply scale the CCSD(T) interaction energies to match the MRCI+Q energies. However as the optimized scale parameter was 1.022, very close to unity, for CO+Ar, we will assume that no scaling is required, just a constant shift in energy. The shift between our calculated MRCI+Q energies and QZ CCSD(T) energies was determined from the CO potential curve, with O 20 a_o from the CO bond mid-point. We performed a leasts squared fit for the diatomic potential as described in the next section, except we included both the QZ CCSD(T) and MRCI+Q data and an additional parameter, a constant shift of the MRCI+Q data. The shift between the QZ CCSD(T) energies and the Schmidt *et al.*[24] MRCI+Q energies was initially estimated from calculations at four identical geometries in the vicinity of the global minimum of the lowest $^3A'$ or $^3A''$ state, but in the end the shift was optimized in the final fit. The shift between the TZ CCSD(T) energies and the Schmidt *et al.* energies was originally determined from averaging over a large number of geometries that the two sets of data had in common, but in the end the shift was also optimized in the final fit. From these comparisons, we estimate that this mixing of the data gives rise to noise at circa 0.1 mE_h, thus it is pointless to try to fit the data better than this.

The second consequence is that it would seem that we cannot base our energy weights on the interaction energy as was done for CO+Ar. Thus we experimented with several other options for getting the weights, and found that the most desirable fits were obtained by basing the weights on the difference between the *ab initio* data and the asymptotic diatomic potential computed using the shortest CO distance, ΔV. In particular we started with $1/\min(\epsilon, \Delta V)$, with $\epsilon = 0.01$ E_h, just as we had done for CO+Ar. Then the weights for energies between 1 and 5 E_h higher than the global minimum were multiplied by 0.1, the weights for energies between 5 and 10 E_h higher than the global minimum were multiplied by 0.01, and the weights for energies above 10 E_h higher than the global minimum were multiplied by 0.001. Finally we divided the weights for the Schmidt *et al.*[24] and TZ CCSD(T) energies by 4 to account for the larger number of data points for those two data sets. We will call these the canonical dataset weights.

The third consequence is the analytic representation is non-linear in all pa-

rameters. This makes the fitting process much more difficult than for CO+Ar. We found that our nonlinear least squares routine would sometimes take parameters into non-physical space, *e.g.* exponential damping parameters would be taken to very large values. When necessary, we constrained the troublesome parameter to fall within a specific range by replacing the parameter p with $p(x) = p_{avg} + \frac{p_{rng}}{\pi}\tan^{-1}(x)$ and optimizing x, with $p_{avg} = \frac{p_l + p_u}{2}$ and $p_{rng} = p_u - p_l$, where p_l and p_u are the upper and lower constraints on p. Occasionally the optimization would send x essentially to $\pm\infty$, in which case we would reset x to zero and re-optimize.

As with the CO+Ar potential, we optimized our parameters by sequence of fits of ever increasing complexity.

For our zero-order fit, we diagonalized a three-by-three matrix with the first two diagonals represented by the CO diatomic potential plus the function of Eq. 1, except that F was taken to be unity, and Ar is replaced with O. The third diagonal was taken to be the O_2 diatomic potential plus the non-bonding CO potentials used for the first two diagonals. We originally took the off-diagonal couplings to be constants, but as soon as we looked at the fit in the C+O+O limit, we realized that the off diagonal coupling should go to zero in the C+O+O limit, so instead we represented them as $C_x \exp(-\alpha_x \rho)$ with C_x and α_x parameters and ρ the hyperradius of the mass scaled Jacobi coordinates of the system. As a reminder, this hyperradius is the same whether CO+O′, CO′+O, or O_2+C mass scaled Jacobi coordinates are used to compute it.

For linear geometries, symmetry requires some of these coupling matrix elements to also be zero to reproduce the conical intersections. However we do not make this restriction for two reasons. First, having these matrix elements go to zero would lead to points on the PES with discontinuous derivatives, and that would cause difficulties with the dynamics calculations. Second, these conical interactions are not isolated, but rather are due to more than two electronic states interacting, and this tends to round over the intersections.

As we did for CO+Ar, we first start with the constraint $C_6^{OC} = C_6^{OO}$, leading to the optimization of a single parameter, and in this fit we utilized only the CO+O′ and CO′+O diabats. Our initial guess for this parameter was taken from our best fit to the diatomic CO potential, see the next section. Before we performed the fit we eliminated all *ab initio* data that gave differences between the data and the fit computed with the initial guess parameter that were less (more negative) than five times the 10th percentile or were greater than five times the 90th percentile of the weighted difference between the data and the fit. This left 7540, 5594, and 6020 data points for the $^3A'$, 1 $^3A''$ and 2 $^3A''$ surfaces, respectively. We then allowed the two parameters to vary freely, but found that the resulting fit was quite insensitive to the value of C_6^{OO}, so we maintained the above constraint until later parts of the optimization. In this fit, we took the parameter δ in Eq. 3 as the value used in the CO+Ar PES.

Next we optimized the parameters α^{OC} and α^{OO} in Eq. 2. In this optimization, we added the C_2+O diabat, and assumed that the values of C_6^{OO} and α^{OO} did not depend on the diabat. The O_2 potential curve was taken from unpublished MRCI calculations using the d-aug-cc-pVTZ basis, shifted so the zero

of energy matched the C+O+O asymptotic limit. We started with the canonical dataset weights, except we excluded points from the fit that were near the global minimum. For the Schmidt *et al.*[24] data, this was done by scanning inward along the non-bonding CO bond length and not including points past the first significant local maximum. For the CCSD(T) and MRCI+Q data, points where the distance between the non-bonding O and CO bond midpoint were smaller than 5 a_{o} were eliminated. Multiple passes through the fitting process were then carried out, with energies with weighted fitting errors more negative than five times the 10th percentile and more positive than four times the 90th percentile eliminated after each pass. This was continued until no more points were eliminated. The choice of factors of four vs. five in this culling was made deliberately to eliminate a single geometry that caused problems.

Once this fit was completed, we lifted the constraint $\alpha = \alpha^{\mathrm{OC}} = \alpha^{\mathrm{OO}}$ and re-optimized the parameters. Then we added the parameter α^x to the mix and optimized it as well. After a fit, we would scan for fitted energies falling below the global minimum of the *ab initio* data for geometries with zero weights. When these were encountered, their weights were reset to 0.1, and the fit was redone until no more such points were found. This is our zero-order fit, and in the final optimization, 3339, 3438, and 2870 data points were kept for the three surfaces, respectively.

At this point we added the fourth diabatic state, *i.e.* the analytic representation is found by diagonalizing a four-by-four matrix, and reset the weights on all points to the canonical dataset weights, thus there were a total of 10352, 6378, and 6678 points with significant weight for the three surfaces. Starting with a simple representation of the new diagonal element, *i.e.* we represent it as the a constant plus the sum of three two-body potentials with each two-body potential consisting of a repulsive Born-Meyer term and an attractive damped dispersion term like in Eq. 3. We take the off diagonal coupling to the other diabats to have the same functional form as the coupling between the first two diabats, albeit ultimately with different parameters. We take as initial guesses for the parameters the analogous parameters from the zero-order fit, and we first optimize the coefficient C_x in the off diagonal coupling for this new diabat. Then we simultaneously optimize it and the five parameters representing the diagonal element of the third diabat. This later optimization was carried out by multiple passes, with energies with weighted fitting errors more negative than six times the 10th percentile and more positive than six times the 90th percentile eliminated after each pass.

We next added a correction of the form

$$\exp\left\{-a_r\left[\left(R_{\mathrm{CO}} - R_m\right)^2 + \left(R_{\mathrm{CO'}} - R_m\right)^2\right] - a_\theta\left(\cos\theta_{\mathrm{OCO'}} - \cos\theta_m\right)^2\right\}$$
$$\times \sum_{ijk} C_{ijk}^{\mathrm{OCO}}\left(R_{\mathrm{CO}} - R_m\right)^i\left(R_{\mathrm{CO'}} - R_m\right)^j\left(\cos\theta_{\mathrm{OCO'}} - \cos\theta_m\right)^k \quad (7)$$

to the fourth diabat, where R_m and θ_m are the CO bond length and OCO angle where the difference between the zero-order fit and *ab initio* data is most

negative. We make the restriction that $i + j + k \leq 4$ for the $^3A'$ and 1 $^3A''$ surfaces and $i+j+k \leq 2$ for the 2 $^3A''$ surface. The coefficients in this expression were optimized, then the off diagonal coupling parameters to the other diabats were optimized. As before, we carried out this optimization by multiple passes, with energies with those weighted fitting errors more negative than six times the 10th percentile and more positive than six times the 90th percentile eliminated after each pass.

Next we added the parameters $C_{ij}^{(n)}$ of Eq. 4 to the diagonals of the CO+O' and CO'+O diabats and optimized them. In this optimization, we made the restriction $i+j \leq 4$, 3, and 2 for the three surfaces, used $p = 1$ in Eq. 4 and used Eq. 5. Then we optimized the C_{ij}^n as well as the Gaussian parameters g and R_1. This also was carried out via multiple passes, with energies with weighted fitting errors more negative than six times the 10th percentile and more positive than six times the 90th percentile eliminated after each pass. The damping parameter d was fixed at 0.1.

At this point, we simultaneously optimized all parameters for all diabats as well as the shifts for the different types of *ab initio* energies and removed the constraints that the parameters for C+O be the same in the C_2+O diabat as the CO+O diabats. Once again we completed multiple passes, with energies with weighted fitting errors more negative than six times the 10th percentile and more positive than six times the 90th percentile eliminated after each pass. This was continued until no more points were eliminated.

Finally we reset all the weights to the canonical dataset weights and re-did the final optimization passes with energies with weighted fitting errors more negative than six times the 10th percentile and more positive than six times the 90th percentile eliminated after each pass. This was continued until no more points were eliminated. Finally there were 10161, 7667, 6809 points with significant weights for the three surfaces.

Because the points were unequally weighted, it is hard to quantify the fitting error with a single number but we obtain 0.075, 0.18, and 0.12 for the weighted average root-mean-square error for the A', first A'', and second A'' surfaces, respectively. This means, for example, that on the first A'' surface, geometries with energies less than 0.01 E$_h$ will have typical errors ϵ times less, *i.e.* 0.0018 E$_h$=1.1 kcal/mol, while geometries with energies higher will have percent errors of a hundred times more, *i.e.* 18 percent.

In Fig. 5 to Fig. 7, we show cuts through the CO+O potentials similar to Fig. 1 for CO+Ar. We plot the analog of V^{int} for CO+Ar, *i.e.* the difference between the full potential and V^{CO} evaluated at the abscissa. However, since we compare to the Schmidt *et al.*[24] data which was laid out on a different grid, rather than using the coordinates of Fig. 1, we use bond-length-bond-angle coordinates with the bond angle fixed at 120 degrees. Because of the different coordinates, the curves do not show the local maxima like in Fig. 1, but we can see from this figure that the fit does a good job of interpolating the *ab initio* data.

In Figs. 8 to 16 we show contour maps of the difference between the full

potential and V^{CO} for r_{vib} shown on the y axis. These plots show the same contours and r_{vib} values that we showed in Fig. 2-4 for CO+Ar, so they can be directly compared. We also show for reference the geometries of the Schmidt *et al.* calculations, as well as our MRCI+Q and CCSD(T) calculations that were used to generate the analytic representation.

First we contrast the CO+Ar PES and the CO+O PESs as a whole, and then we compare the different CO+O PESs. For bond lengths near the CO equilibrium geometry, *i.e.* Figs. 2 and 8-10, we see some similarities and some differences. We see that CO+O has more long range attraction then we see in CO+Ar, but the lower part of the repulsive part of the PESs are not that dissimilar. The higher parts of the repulsive regions are quite different between CO+Ar and CO+O: we see that an O atom can get much closer to CO than the Ar atom can. Also an O atom can get closer to the CO bond midpoint than to either the C or O end of CO, which the reverse of the situation for CO+Ar. But perhaps the biggest difference occurs in the intermediate repulsive region: for Ar, the transition from lower repulsion to higher repulsion is smooth, whereas for O, there is local minima on the $^3A'$ and lowest $^3A''$ surface, and all CO+O surfaces show some sort of flatness in the intermediate region.

Moving on to $r_{vib} = 3$, *i.e.* Figs. 3 and 11-13, we see that the similarities between CO+Ar and CO+O have decreased: the lower parts of the repulsive part of the PES are much more compact for CO+O, and in fact, for sideways approach on the lowest $^3A''$ PES, there is no lower part of the repulsive potential before the local minimum. The local minima on the CO+O PESs have gotten significantly deeper, and although the CO+Ar PES shows some ability of the Ar atom to get closer to the CO bond midpoint than to either the C or O end of CO, on the CO+O PESs, we see a narrow range where the O atom can get significantly closer to the CO bond midpoint than to either the C or O end of CO.

If we stretch the CO bond length to $r_{vib} = 4$, Figs. 4 and 14-16, we see that now the CO+O PESs have a strongly attractive ring around the CO and high energy O atoms can actually get to the CO bond midpoint.

Let us now compare and contrast the different CO+O PESs. The highly repulsive parts of all three PES are very similar, and the strongly bound parts of the $^3A'$ and lowest $^3A''$ surface are also very similar. In the weakly bound and weakly repulsive part, the second $^3A''$ surface tends to show more extended repulsion, and the lowest $^3A''$ surface tends to show more extended attraction, while the $^3A'$ surface is intermediate in both categories. Now due to the differences in weak repulsion on the three CO+O PESs, it is interesting to consider a cut through the local minimum.

6 CO potential curve

For our dynamics calculations, we wish to use as accurate as possible CO vibrational potential. This means for CO+Ar, we will add this vibrational potential to V^{int} to have the full potential. For CO+O, we will substitute the accurate

CO vibrational potential for the vibrational potential we used in the CO+O'
and CO'+O diagonal matrix elements. It should be noted, that in this substitu-
tion, the accurate diatomic potential must be shifted to match the asymptotic
energy of the vibrational potential used to generate the analytic representation.

Perhaps the most accurate published potential energy curve for CO is that
due to Coxon and Hajigeorgiou[33], who generated a analytic representation
based on reproducing very accurate spectroscopic data for the CO molecule via
accurate numerical solutions of the ro-vibrational problem. However they forced
the long range part of the potential to go as r_{vib}^{-5}, consistent with quadrapole-
quadrapole interaction, which on face value is appropriate for atomic states
that both have nonzero quadrapole moments. However we have analyzed the
result of extensive *ab ititio* calculations on the CO molecule, and find that the
asymptote where the two electronic angular momenta couple[34] to form $L = 2$
indeed has quadrapole-quadrapole interaction, but the asymptote where the two
electronic angular momenta couple to form $L = 0$ has no quadrapole-quadrapole
interaction. The ground $^1\Sigma^+$ state correlates to the latter and the first excited
state correlates to the former. This does lead to a large r_{vib} curve crossing, but to
simplify the treatment, we assume the nuclear dynamics will behave diabatically
in this region, thus we force the long range part of the adiabatic potential to
go as r_{vib}^{-6}. Therefore, we decided instead to use a calculated potential energy
curve to represent the CO molecule for our PESs.

In order to be as accurate as possible, our calculated potential is based on the
ACPF method, correlating all electrons, with a very large one-electron basis. We
used the aug-cc-pV5Z basis for C and the d-aug-cc-pV5Z basis for O, with only
the p functions contracted. To this basis we added the extra tight $pdfgh$ core-
valence correlating basis functions of Schwenke.[35] The molecular orbitals were
determined from state-averaged MCHF calculations that keep the three lowest
a_1 orbitals doubly occupied and included an active space consisting of three a_1
orbitals and two each of b_1 and b_2 orbitals. We used the dynamic weighting
scheme of Deskevich *et al.*[23] with energy parameter 2 eV^{-1}, and included 14
$^3A_1$ states, 17 $^3B_1$ and $^3B_2$ states, and 15 $^3A_2$ states in the state averaging
process. In the ACPF calculations, we correlated all electrons, and used the
second order Douglas-Kroll-Hess method[26][27] to include scalar relativistic
effects.

We represent the diatomic CO potential curve by the form

$$V^{\mathrm{CO}} = V^{\mathrm{LR}} + V^{\mathrm{SR}} + V^{\mathrm{in}}, \tag{8}$$

where the long range term is given by

$$V^{\mathrm{LR}} = C_\infty - C_6/(r^6 + \delta^6), \tag{9}$$

the short range term is given by

$$V^{\mathrm{SR}} = 48 \exp(-\alpha r)/r, \tag{10}$$

and the intermediate range term is given by

$$V^{\mathrm{in}} = r^n \exp(-ar) \sum_{i=0,n_x} \mathcal{C}_i (r - r_m)^i, \tag{11}$$

and r is the bond length. We determined the long range coefficients C_∞ and C_6 by a least squares fit to the large r data points, with the fitting weights being r^2. The damping parameter δ and the short range parameter α were determined simultaneously fitting the small r data points to the sum $V^{\mathrm{SR}} + V^{\mathrm{LR}}$. In this fit, we started with an initial guess for δ, then fit $\{\log[(V - V^{\mathrm{LR}})r/48]\}/r$ to a constant. Then we varied δ to minimize the error in the fit. Finally, we performed fits to determine the linear coefficients in $\mathcal{C}_i$. We only fit energies less than C_∞, but we used unit weights for these energies. We chose the exponential parameter a as r_m/n, where r_m was the lowest energy geometry in the input data. This ensures that the maximum of $r^n \exp(-ar)$ occurs at r_m. We then varied n by hand to minimize the fitting error when $n_x = 4$. This yielded $n = 9$. We then fixed n and increased n_x to get our final fit, and the final value of n_x was 11.

In Fig. 17 we compare our analtyic representation of the 5Z all-electron ACPF calculations to that of Coxon and Hajigeorgiou.[33] In this figure, the abscissa covers 0.86-2.00 Ångstrom, the range over which Coxon and Hajigeorgiou thought their potential was well constrained by spectroscopic data. In the scale of this figure, the two curves are virtually indistinguishable, except at the upper right hand end of the curves: this reflects the different long range form of the two potentials.

Our computed r_e is 1.128908 Å (2.133327 a_o) while that from Coxon and Hajigeorgiou is 1.128229476 Å, and our computed D_e is 90563 cm^{-1} vs. their value of 90674.0 cm^{-1}.

7   Stationary Points

Qualitative models of dynamics require as input the various stationary points, minima and transition states, thus we have computed these for the present OCO PESs.

The stationary points were found as follows: a three dimensional grid of points in r_{vib}, $x = R_c \sin\theta_c$, $y = R_c \cos\theta_c$ space was generated, and at each point on the grid, the magnitude of the gradient of the potential was minimized using the downhill simplex method[32] followed by polishing with Powell's method.[32] The gradient was computed analytically. Each unique geometry with zero gradient was then analyzed to determine the normal mode frequencies. The Hessians were computed numerically using central difference formulas for multiple step sizes and extrapolated with polynomials to zero step size. In all calculations, we used the PESs with the CO vibrational potential from Sect. 6 replacing the *ab initio* one.

All energies are reported with the zero of energy being the minimum of the CO vibrational potential. The O+C+O dissociation limit is at 11.22 eV (258.9 kcal/mol), and the C+O$_2$ asymptote is at 6.139 eV (141.6 kcal/mol). The asymptotic CO harmonic frequency is 2172 cm^{-1} and the asymptotic O$_2$ harmonic frequency is 1547 cm^{-1}.

The $^3A'$ PES has a minimum in the strong interaction region: it has depth

0.7768 eV (17.91 kcal/mol) and occurs when $R_{CO} = R_{CO'} = 2.348\ a_o$ and $\theta_{OCO'} = 128°$ and has normal mode frequencies of 528, 1027, and 1417 cm^{-1}. The $1\,^3A''$ PES also has a minimum, but its depth is only 0.2996 eV (6.91 kcal/mol), but it occurs at a similar geometry: $R_{CO} = R_{CO'} = 2.359\ a_o$ and $\theta_{OCO'} = 128°$ while the normal mode frequencies are 148, 712, and 1388 cm^{-1}. The $2\,^3A''$ PES shows no triatomic minimum with depth greater than 1 kcal/mol.

On the $^3A'$ and $1\,^3A''$ PESs, the transition states for the homogenous exchange reaction are very similar and have fairly low barriers: only 0.191 eV (4.4 kcal/mol) with $R_{CO} = 2.138(2.138)\ a_o$, $R_{CO'} = 3.554(3.498)\ a_o$ and $\theta_{OCO'} = 121(126)°$ and imaginary frequency of 340(439) cm^{-1}, where first number is for the $^3A'$ PES and the number in parenthesis is for the $1\,^3A''$ PES. The remaining vibrational frequencies are 325 (342) and 2145 (2145) cm^{-1} for the two surfaces.

On the $2\,^3A''$ PES, the homogenous exchange reaction transition state barrier is significantly greater, at 2.41 eV (55.8 kcal/mol). The geometry is also very different, having $R_{CO} = R_{CO'} = 2.469\ a_o$ and $\theta_{OCO'} = 123°$ with an imaginary frequency of 1564 cm^{-1} and vibrational frequencies 221 and 1117 cm^{-1}.

The transition state for the formation of O_2+C is in the exit channel on the $^3A'$ PES, occurring when $R_{CO} = R_{CO'} = 6.441\ a_o$ with an OO bond length of 2.299 a_o, which is very close to the asymptotic O_2 minimum geometry of 2.297 a_o. The barrier height is only 0.04 eV (1.0 kcal/mol) above the O_2+C asymptote, and the imaginary frequency is 71 cm^{-1}, with vibrational frequencies of 50 and 1541 cm^{-1}. On the $^3A''$ PESs, the situation is different. For the first state, there are two transition states separated by a hill top, with the first occurring at $R_{CO} = R_{CO} = 3.031\ a_o$, $R_{OO} = 2.414\ a_o$ with barrier height 5.85 eV, or 0.10 eV above the O_2+C asymptote, and the second occurring at $R_{CO} = 2.768\ a_o$, $R_{CO'} = 4.528\ a_o$, $R_{OO'} = 2.492\ a_o$ with height 5.93 eV, or 0.20 eV above the O_2+C asymptote. The imaginary frequencies of the two transition states are 774 and 1177 cm^{-1} respectively, and the vibrational frequencies are 332 and 850 cm^{-1} for the first transition state and 175 and 816 cm^{-1} for the second transition state. The hill top separating the two transition states occurs at $R_{CO} = 2.763$, $R_{CO'} = 3.807$, and $R_{OO} = 2.552\ a_o$ with height 6.00 eV, or 0.24 eV above the O_2+C asymptote. The imaginary frequencies are 1159 and 222 cm^{-1}, while the vibrational frequency is 869 cm^{-1}. The second $^3A''$ PES only has a single transition state occurring at $R_{CO} = R_{CO} = 4.227\ a_o$, $R_{OO} = 2.354\ a_o$ and has barrier height of 7.45 eV, or 1.3 eV above the O_2+C asymptote. The imaginary frequencies is 341 cm^{-1} and the vibrational frequencies are 61 and 1333 cm^{-1}.

8   Dissociation Dynamics

Because of the very large number of bound ro-vibrational states of X $^1\Sigma^+$ CO - we obtain 13754 ro-vibrational levels on our CO potential curve - we had to sample preferentially from higher lying levels to obtain accurate rate coefficients over the entire temperature range.

We have used the above potential energy hyper-surfaces to carry out quasi-classical trajectory calculations of the thermal equilibrium dissociation rate coefficient for CO+Ar. The quasi-classical trajectories calculations were carried out using the trajectory code VVTC[30] (Vectorized Variablestepsize Trajectory Code). In these calculations, we sampled the relative translational energy and impact parameter as part of the Monte-Carlo integration over the CO angle variables. The impact parameter was chosen in an efficient manner via stratified sampling.[36] In our initial calculations, we sampled the initial ro-vibrational levels of CO from the complete list of bound and quasi-bound levels determined from the WKB calculations.[30] This involved J from 0 to 293 and v from 0 to a maximum value of 83 for $J = 0$, for a total of 13754 levels. For CO+Ar, even though we ran over 700,000 trajectories for each temperature, we could only find dissociating trajectories for T> 10000 K.

Thus to improve our sampling statistics, we consider calculations where lower energy ro-vibrational levels were excluded from the sampling. We considered three such choices: first we only considered long lived quasi-bound levels, $i.e.$ levels with predicted lifetimes[30] greater than 200 ps. Second we included those levels plus all bound levels with energies within 0.1 E_h of the dissociation limit. Finally we added the bound levels with energies within 0.2 E_h of the dissociation limit. The four sets of results are shown in Fig. 18. One can see that the results from the calculations sampling just from long-lived quasi-bound levels are much too low, while on the high-T side of the plot where all the other sampling techniques give converged results, the other methods give very similar results. As T goes down, the 0.1 and 0.2 E_h sampling results agree very well until the error bars for the later results begin to grow. Thus we conclude that sampling just including levels within 0.1 E_h of the dissociation limit provides a proficient and reliable means for computing the equilibrium dissociation rate coefficients. We fit the CO+Ar dissociation rate coefficient to the function $2.781 \times 10^{-5} T^{-0.8514} \exp(-128741.4\,\mathrm{K}/T)$, and this is also shown in the figure. In this fit, we fixed the exponential parameter the value of D_0 obtained from our computed CO diatomic potential as described in the previous section. See the discussion section for more information about this fit.

We carried out similar tests for the CO+O PESs, and found very similar results. In Fig. 19, we show the results for the equilibrium dissociation rate coefficients for the three different CO+O PESs, as well as the average and our fit to the average. The average is the physically relevant quantity. The $^3A'$ and $2^3A''$ surfaces give rate coefficients that are quite similar, while the $1^3A''$ gives a rate coefficient that is about twice the sum of the results for the other two surfaces. We fit the average to the function $0.1733 T^{-1.71} \exp(-128741.4\,\mathrm{K}/T)$.

We also carried out calculations for CO+O where we again sampled from all the CO levels to get estimates of the rates for homogeneous exchange reactions and reactions that form O_2+C. Since the homogeneous exchange reaction has a very low barrier, this reaction is quite fast, we were able to get good statistics for all temperatures with 200000 trajectories, but not so for the exchange reaction to form O_2+C. Increasing the number of trajectories to 600000 did not significantly improve the situation. For this case we sampled from bound

energy levels within 0.25 E_h of the dissociation limit plus all long-lived quasi bound levels. The calculated rate coefficients for this case were within 65-75% of the values obtained by sampling all levels for temperatures between 12,000 and 20,000 K and appear to be well behaved down to 5000 K. The rate coefficients for exchange reactions are discussed in the next section.

9   Discussion

During a typical scenario of a spacecraft entering the Martian atmosphere, the shock that forms in front of the vehicle is characterized by a rapid increase in pressure and temperature of the atmospheric gas. The vibrational and electronic modes of the gas are excited more slowly, so the translational temperature overshoots the thermal equilibrium value because it reflects all the energy generated by the compression of the gas. For an entry speed of 8 km/s, the time for the translational temperature to rise from the free stream to the peak value is about 1 μs, corresponding to a shock thickness of ≤ 1 cm. Full relaxation of the internal energy modes occurs in 1-5 μs (local thermal equilibrium) and chemical relaxation time is generally 10-20 μs. The dissociation of CO_2 into CO $(^1\Sigma^+)$ and $O(^3P)$ is immediate and complete for entry speeds above 5 km/s. On the other hand, CO dissociation is relatively slow and incomplete. Initially the collision partners for the latter process are atomic oxygen and other CO molecules, which formed with equal mole fractions from CO_2 dissociation. As CO and N_2 slowly dissociate, N and C mole fractions increase. Their contribution to CO dissociation is not considered in the present study. However, the reaction between CO and O which forms molecular oxygen,

$$CO + O \rightarrow C + O_2, \tag{12}$$

followed by rapid dissociation of O_2 provides an alternate two-step pathway for CO dissociation. The endothermicity of this reaction is about 6.123 eV which is only 54% of the CO bond energy. The Park model[3] includes these reactions.

Our rate coefficients for collisional dissociation of CO by collision with argon and oxygen atoms are in rough agreement with the published shock tube experiments, all of which date to before 1993. The experiments to determine dissociation rate coefficients for CO/Ar mixtures were carried out by Davies[11], Appleton *et al.*[12](who also used $CO/O_2/Ar$) and Mick *et al.*[13] Determinations for pure CO were carried out by Presley *et al.*[14], Chackarian[15] and Hanson[16]. All the data up to 1974 are tabulated and compared in the compendium by Baulch *et al.*[17] who included their recommended Arrhenius rate coefficient expression, which is mostly based on the experiments of Davies and Appleton *et al.* That compendium also tabulated relative dissociation efficiencies for different CO collision partners relative to CO + Ar, i.e., rate coefficient ratios $k_{diss}^{CO+CO}/k_{diss}^{CO+Ar} = 1 - 2$ and $k_{diss}^{CO+O}/k_{diss}^{CO+Ar} = 15$. The ratio for $k_{diss}^{CO+O}/k_{diss}^{CO+Ar}$ comes primarily from Appleton *et al.*, but the recommendation for $k_{diss}^{CO+O}/k_{diss}^{CO+Ar}$ is not really supported by the experiment. There is insufficient data to ascertain the temperature dependance of this ratio, so they are

18

considered to be independent of temperature. Various methods were used to monitor reaction progress: 117.6 nm VUV and IR emission from CO, atomic resonance absorption spectroscopy, pressure variation and C_2 Swan emission (C_2 being formed by secondary reaction of CO with carbon atoms).

Unless stated otherwise, the comparisons between these different experiments and our calculated rate coefficients are based on the published Arrhenius fits to the experimental data. For CO + Ar and CO + O the relevant experimental data are given in Figs. 20 and 21, respectively, along with the results from the present work. All of the Arrhenius fits of the rate coefficient data are given in Table 1. We have determined dissociation rate coefficients for thermal equilibrium conditions, whereas the rate coefficients extracted from the experimental data are for quasi-steady state conditions which may differ from thermal equilibrium. At high temperatures, *i.e.*, greater than 15000 K, we expect the steady state rate coefficients to be 2-5 times smaller than the thermal equilibrium values, as has been demonstrated in detailed master equation studies of N_2 dissociation (Panesi *et al.*[37], Valentini *et al.*[38]). It can be seen that the agreement between these various determinations is fairly good at temperatures between 8500 K and 12,000 K. Also shown in figure 20 for CO+Ar and figure 21 for CO+O are the rate coefficients recommended by Baulch *et al.*[17], the rate coefficients used in the Park model[3] and the new Johnston and Brandis model[18] discussed below. Davies[11], Appleton et al.[12] and Mick *et al.*[13] used CO-Ar mixtures for their shock tube experiments with the initial CO mole fraction ≤0.05. At 9000 K, the highest temperature run in the Mick *et al.* study, the rate coefficients for Mick *et al.* and Davies are 3.5 times smaller and 2.0 times larger, respectively, than the Appleton *et al.* rate coefficient. Throughout the temperature range 7000 K to 20,000 K the Appleton *et al.* rate coefficients are bracketed by the Davies and Mick *et al.* values, but the relative differences between them are larger for lower temperatures. In the Appleton *et al.* study O_2 was added to the CO-Ar mixture for some runs so the CO dissociation rate coefficient for CO + O collisions could also be determined. The other shock tube studies[14, 15, 16] used pure CO and measured dissociation of CO due to CO, C and O collisions. Chackerian also attempted to determine rate coefficients for CO + CO collisions by analyzing the data at short times immediately after the shock and for CO + C and O collisions at longer times. Appleton *et al.*[39] previously had used this approach for determining dissociation rate coefficients for N_2 + Ar, N_2 + N_2 and N_2 + N from shock tube experiments using N_2-Ar mixtures. In the experiments carried out with pure CO, the rate coefficients for CO + O and CO + C could not be differentiated.

A different approach was taken by Park[4, 6, 7, 5, 3] in formulating 2-T chemical kinetics models to describe the non-equilibrium flows observed in the shock tube experiments and during hypersonic entry of spacecraft into planetary atmospheres. Park used separate vibrational and translational temperatures to enable simulations to account for the slower relaxation across a shock of vibration and electronic energy modes, compared to translation and rotation. Park created empirical dissociation rate coefficients using an average temperature

$(T_{ave} = (TT_{vib})^{1/2})$ in the three-parameter Arrhenius expression

$$k_{diss}(T, T_{vib}) = AT_{ave}^n \exp(-T_{rxn}/T_{ave}), \qquad (13)$$

where A is a constant, n is the temperature coefficient and T_{rxn} is the characteristic reaction temperature based on the dissociation energy. As the system reaches thermal equilibrium, $T_{ave} \to T$ and the expression reduces to the familiar Arrhenius form. For CO_2 and CO dissociation and the exchange reactions $CO + C \to O + C_2$ and $CO + N \to O + CN$, Park calibrated the Arrhenius A parameters to best reproduce the radiative emission from a CO_2-Ar mixture in a reflected shock experiment. The relevant band systems for these reactions[3] were CO_2 IR emission for CO_2 dissociation, CO 4th positive radiation for CO dissociation, C_2 Swan radiation for CO + C and CN violet radiation for CO + N exchange reaction. Previously, Park showed that using T_{ave} in the Arrhenius expression for dissociation rate coefficients worked well if the temperature parameter n is small[7], so for the CO_2 and CO dissociation reactions he set it to unity and adjusted A so the resulting rate coefficient at 10,000 K matched the published value of choice. For CO dissociation that was the dissociation rate coefficient determined by Hanson[16]. The resulting collision partner efficiencies, based on Baulch *et al.*[17] for Ar:O and Hanson for CO:O are Ar:CO:O = 1:10:15.

Recently, Johnston and Brandis[18] repeated this procedure for three dissociation reactions (CO_2, CO and C_2) and two exchange reactions (CO + N mentioned above and $CN + O \to NO + C$) in the Park Mars chemistry model[3], fitting the A parameters to best reproduce spectra of the CO_2 and CO IR emission, CO 4th positive VUV emission and CN violet emission as recorded in the NASA Ames Electric Arc Shock Tube (EAST) facility[40]. To make this comparison, the authors used the coupled flowfield-radiation solver LAURA/HARA[41, 42, 43, 44]. They created a new baseline Mars chemistry model that included their newly calibrated rate coefficients along with updates of some other parameters based on more recent work since the Park model was presented in 1994[3]. The most significant finding of this work is the observation that use of the Park model leads to greater CO 4th positive intensity than is seen in the EAST spectra and that faster removal rates for CO are required to obtain satisfactory agreement between flow field computation and experiment. Johnston and Brandis kept the relative collision partner efficiencies used by Park, but increased all the dissociation rate coefficients by a factor of 5.2.

It should be noted that most of the Arrhenius fits of the experimental data were obtained by assuming T_{rxn} equals the CO bond dissociation temperature, which was taken as 129,000 K. This value was the accepted value when the Park model was created, however a more accurate value is now available: this is 130462 K.[33] Thus, only the parameters A and n were fit to the measured data (T, k_{diss}(T)). For some of the experiments, Refs. [11],[12], and [16], an alternate fit was used with n=0. In these cases T_{rxn} is always lower than the bond dissociation temperature. For a given experiment, the quality of these two fits are comparable. So there is no reason to pick one Arrhenius expression over the other.

A straightforward comparison of the experimental data and our computed rate coefficients for CO+Ar is given in Fig. 22. It can be seen that the results of the present study are in good agreement with the data from Mick *et al.*[13] and the lower temperature data of Appleton *et al.*[12]. The agreement with the results of Davies [11] is less satisfactory. Overall, our rate coefficients agree with the aggregate experimental data for temperature between 6000 and 15,000 K. We have fit our calculated rate coefficients to both two- and three-parameter Arrhenius expressions in the same manner as was done for the experimental data, *i.e.*, the dissociation temperature is fixed for the 3-parameter fit. For our PESs, the CO dissociation energy (D_0) is 11.242 eV, equivalent to T_{diss} = 128,741.4 K. The best experimentally determined value is 128,901 K [33]. The resulting rate coefficient parameters are given in Table 1 and the Arrhenius expressions are shown in Figures 20 and 21. The fits were determined from the calculated rate coefficients over the temperature range 7500-20,000 K. There is a noticeable change in curvature at higher temperatures and the low-temperature data (5000-7000 K) show scatter due to larger statistical errors in the Monte Carlo sampling. The rate coefficient data and Arrhenius fits for both CO+Ar and CO+O (average of values for the three PESs) are shown in Fig 23. The 3-parameter fits are preferred because they better represent the rate coefficients when extrapolated to to full temperature range of the data. It can also be seen that the temperature dependences of the CO+Ar and CO+O rate coefficients are different. The CO+Ar rate coefficients have a steeper slope.

In order to make detailed comparisons between the results of the present study and the previous work we plot the ratios of rate coefficient fits from the older work to the QCT values in Fig 24 for CO = Ar and Fig 25 for CO + O. These ratios are computed from the Arrhenius fits. For the experimentally determined rate coefficients, the ratios are only shown for the temperature range of the experiments. The overall agreement between the present study and previous work is rather good for CO+Ar as all the ratios are between 0.3 and 2.0. The values from experiment have fairly steep slopes, indicating a different temperature dependence. The 3-parameter expression of Appleton et al.[12] is in closest agreement with the QCT fit over the entire temperature range. Note that the Park model[3] uses rate coefficients that are approximately a factor of three lower than ours and the Johnston and Brandis model[18] a factor of 1.5-2 higher. For CO+Ar the situation is problematic. The computed rate coefficients are generally much smaller than the experimentally determined values and the values used in the Park and Johnston and Brandis models. These differences are more pronounced at lower temperatures. Another way to consider the our computed rate coefficients is to examine the ratio of CO+O to CO+Ar dissociation rate coefficients. This is shown in Fig 26. The values for $T \leq 10,000$ K vary between 2 and 8, much smaller than the constant value of 15 chosen by Park and used by Johnston and Brandis. An explanation for the apparent disagreement between our study and previous work is presented below.

Our QCT calculations for CO + O collisions also can be used to obtain rate

coefficients for the exchange reaction (Eq. 12) and

$$CO + O' \rightarrow CO' + O, \tag{14}$$
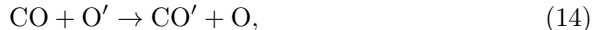
where the $'$ is used to distinguish the two oxygen atoms. The latter process (homogeneous exchange) has a very low energy barrier (about 5 kcal/mol) and thus its rate coefficient is quite large for the entire 5000-35,000 K temperature range of the present study. This reaction, while not changing the chemical composition of the gas, results in faster translational to ro-vibrational energy transfer between the collision partners than would occur due to inelastic collisions alone. The other exchange process, Eq. 12, is endothermic by 6.123 eV and provides an additional channel for removal of CO molecules, as the nascent oxygen molecules should readily dissociate at these temperatures. The rate coefficients for this exchange reaction are shown in Fig. 27 along with the direct dissociation and overall CO removal rate coefficients. Also shown are the rate coefficients from shock tube experiment of Dean *et al.*[45] and the corresponding value in the Park model[3]. It can be seen that the exchange reaction is faster than direct dissociation for temperatures up 16,000 K and, therefore dominates the removal of CO molecules throughout the temperature range of the shock tube experiments. Dean *et al.* actually studied this reaction in the reverse (exothermic) direction for temperatures between 1500 and 4200 K. They comment that the atomic oxygen product may be formed in either the ^{3}P or ^{1}D state. The corresponding rate coefficient in the Park model[3] is attributed to a paper by Thorne *et al.*[46] that describes a model for hydrocarbon kinetics. The Arrhenius parameters for this reaction are listed in a table of 163 reactions without references to the original work. Thus, the accuracy of these published values for the exchange rate coefficient is questionable. Also shown in Fig.27 is the CO removal rate coefficient given as the sum of dissociation and exchange reactions. This corresponds to the quantity actually measured as CO dissociation in the shock tube experiments of Appleton *et al.* and others.

Figure 26 shows the ratio of CO + O to CO + Ar rate coefficients. When exchange and dissociation are combined, this ratio is very large at low temperature and tends toward unity for temperatures greater than 20,000 K. For the temperature range of interest to Mars entry (6000-8000 K), it has values greater than 25. In contrast, the ratio for dissociation without exchange varies between 3.0 and 4.3 over these temperatures. A 2-parameter Arrhenius fit of the computed exchange reaction rate coefficient data between 5000 and 10,000 K results in the following expression for this reaction: $k_{exch}^{CO+O} = 5 \times 10^{-10} \exp(-77600/T)$. The reaction temperature is equivalent to 6.69 eV, which is 0.57 eV larger than the endothermicity.

10   Conclusions

We have carried out first principles quasi-classical trajectory calculations of the thermal dissociation rate coefficients for CO+Ar and CO+O over a wide temperature range using new potential energy surfaces. Our results are not really

consistent with the intepretation of the 20-45 year old experimental data. We find the ratio between rate coefficients for dissociation due to O-atom and Argon collisions is considerably smaller than the conventional value of 15. Also, it is not constant with respect to temperature (as assumed previously), varying from 1.5 to 3.3 over the temperature range considered by the experiments. Also our rate coefficients show considerably less curvature on an Arrhenius plot than the published values. Our calculations do not support the recent upward adjustment of the CO dissociation rate coefficients made by Johnston and Brandis,[18] which was made to improve the prediction of CO 4th-positive radiation observed in test facilities at NASA Ames Research Center.

We also computed the thermal reaction rate coefficients for the CO + O exchange reaction that produces C + O_2. We find this reaction to be faster than collisional dissociation for temperatures below 16,000 K, and especially so below 10,000 K. This reaction is endothermic by 6.123 eV (only 54% of the CO dissociation energy) and with the subsequent collisional dissociation of the O_2 product provide an alternative dissociation pathway for CO.

Because of phenomenological adjustments to the Mars chemistry model, the use of the presented dissociation and exchange rate coefficients instead of the values in the Park model[3] or the new Johnston and Brandis model for simulations of spacecraft entering the Martian atmosphere will not necessarily result in improved agreement between simulations and measurements. However this would most likely indicate problems with other reaction rate parameters rather than problems with the rate coefficients determined in the present work. Nonetheless, we recommend that the computed dissociation and exchange rate coefficients computed in the present study be used in place of the values in the Park model[3] and the new Johnston and Brandis model for simulations of spacecraft entering the Martian atmosphere. Preliminary testing of the new rate coefficients in Mars entry simulations have shown very promising results,[47] suggesting that the physics in the Mars chemistry model is nearing a very solid foundation.

References

[1] Mahaffy, P. R.; Webster, C. R.; Atreya, S. K.; Franz, H.; Wong, M.; Conrad, P. G.; Harpold, D.; Jones, J. J.; Leshin, L. A.; Manning, H.; Owen, T.; Pepin, R. O.; Squyres, S.; Trainer, M.; MSL Science Team *Science* **2013**, *341*, 263–266.

[2] Seiff, A.; Kirk, D. B. *J. Geophys. Res.* **1977**, *82*, 4364–4378.

[3] Park, C.; Howe, J.; Jaffe, R.; Candler, G. *J. Thermophys. Heat Trans.* **1993**, *7*, 385–398.

[4] Park, C. *J. Thermophys. Heat Trans.* **1988**, *2*, 8–16.

[5] Park, C. *J. Thermophys. Heat Trans.* **1989**, *3*, 233–244.

[6] Park, C.; *Two-Temperature Interpretation of Dissociation Rate Data for N_2 and O_2*; AIAA Paper AIAA-88-0458; 1988.

[7] Park, C. *AIAA-89-1740* **1989**.

[8] Landau, L.; Teller, E. *Theory of sound dispersion*, 1936; Vol. 10.

[9] Park, C. *Nonequilibrium Hypersonic Aerothermodynamics*; J. Wiley, New York, 1990.

[10] Brandis, A. M.; Johnston, C. O.; Cruden, B. A.; Prabhu, D. K.; Wray, A. A.; Liu, Y.; Schwenke, D. W.; Bose, B. *Journal of Quantitative Spectroscopy and Raiative Transfer* **2013**, 91–104.

[11] Davies, W. O.; *Radiative Transfer on Entry into Mars and Venus*; NASA report NASA CR-58574; 1964.

[12] Appleton, J. P.; Steinberg, M.; Liquornik, D. J. *J. Chem. Phys.* **1970**, *52*, 2205–2221.

[13] Mick, H.-J.; Burmeister, M.; Roth, P. *AIAA J.*, *31*, 671.

[14] Presley, L. L.; Chackerian, C.; Watson, R.; *The Dissociation Rate of Carbon Monoxide between 7,000 and 15,000 K*; AIAA Paper AIAA-66-518; 1966.

[15] Chackerian, C.; *The Dissociation of Shock Heated Carbon Monoxide Studied by two Wavelength Infrared Emission*; 1971.

[16] Hanson, R. K. *J. Chem. Phys.* **1974**, *60*, 4970–4976.

[17] Baulch, D. L.; Drysdale, D. D.; Duxbury, J.; Grant, S. J. *Evaluated Kinetic Data for High Temperature Reactions*; Butterworths, London, 1976; Vol. 3.

[18] Johnston, C.; Brandis, A. *J. Quant. Spect. Rad. Transfer* **2014**, *149*, 303–317.

[19] Jaffe, R. L.; Schwenke, D. W.; Panesi, M. **2015**, 103–158.

[20] Chaban, G. M.; Jaffe, R. L.; Schwenke, D. W.; *unpublished*.

[21] Werner, H.-J.; Knowles, P. J. *www.molpro.net*.

[22] Kendall, R. A.; T. H. Dunning, J.; Harrison, R. J. *J. Chem. Phys.* **1992**, *96*, 6769.

[23] Deskevich, M. P.; Nesbitt, D. J.; Werner, H.-J. *J. Chem. Phys.* **2004**, *120*, 7281–7289.

[24] Schmidt, J. A.; Johnson, M. S.; Schinke, R. *Proceeding of the National Academy of Sciences* **2013**, *110*, 17691–17686.

[25] Frisch, M. J.; Trucks, G. W.; Schlegel, H. B.; Scuseria, G. E.; Robb, M. A.; Cheeseman, J. R.; Scalmani, G.; Barone, V.; Mennucci, B.; Petersson, G. A.; Nakatsuji, H.; Caricato, M.; Li, X.; Hratchian, H. P.; Izmaylov, A. F.; Bloino, J.; Zheng, G.; Sonnenberg, J. L.; Hada, M.; Ehara, M.; Toyota, K.; Fukuda, R.; Hasegawa, J.; Ishida, M.; Nakajima, T.; Honda, Y.; Kitao, O.; Nakai, H.; Vreven, T.; Montgomery, J. A., Jr.; Peralta, J. E.; Ogliaro, F.; Bearpark, M.; Heyd, J. J.; Brothers, E.; Kudin, K. N.; Staroverov, V. N.; Kobayashi, R.; Raghavachari, J. N. K.; Rendell, A.; Burant, J. C.; Iyengar, S. S.; Tomasi, J.; Cossi, M.; Rega, N.; Millam, J. M.; Klene, M.; Knox, J. E.; Cross, J. B.; Bakken, V.; Adamo, C.; Jaramillo, J.; Gomperts, R.; Stratmann, R. E.; Yazyev, O.; Austin, A. J.; Cammi, R.; Pomelli, C.; Ochterski, J. W.; Martin, R. L.; Morokuma, K.; Zakrzewski, V. G.; Voth, G. A.; Salvador, P.; Dannenberg, J. J.; Dapprich, S.; Daniels, A. D.; Farkas, .; Foresman, J. B.; Ortiz, J. V.; Cioslowski, J.; Fox, D. J.; *Gaussian09 Revision D.01*; Gaussian Inc. Wallingford CT 2009.

[26] Douglas, M.; Kroll, N. M. *Annuals of Physics* **1974**, *82*, 89.

[27] Hess, B. A. *Physical Review A* **1985**, *32*, 756.

[28] Werner, H.-J.; Knowles, P. J. *J. Chem. Phys.* **1988**, *89*, 5803–5814.

[29] Truhlar, D. G.; Brown, F. B.; Schwenke, D. W.; Steckler, R.; Garrett, B. C. *Comparison of ab inito Quantum Chemistry with Experiment: State of the Art* **1985**, 95.

[30] Schwenke, D. W. *Journal of Chemical Physics* **1988**, *89*, 2076–2091.

[31] Hamilton, I. P.; Light, J. C. *Journal of Chemical Physics* **1986**, *84*, 306–317.

[32] Press, W. H.; Teukolsky, S. A.; Vetterling, W. T.; Flannery, B. P. *Numerical Recipes*; Cambridge University Press, New York, 1992.

[33] Coxon, J. A.; Hajigeorgiou, P. G. *Journal of Chemical Physics* **2004**, *121*, 2992–3008.

[34] Schwenke, D. W. *Journal of Chemical Physics* **2015**, *142*, 144107–1440117.

[35] Schwenke, D. W. *Molecular Physics* **2010**, *108*, 2751–2758.

[36] Blais, N. C.; Truhlar, D. G. *Journal of Chemical Physics* **1976**, *65*, 5335.

[37] Panesi, M.; Jaffe, R. L.; Schwenke, D. W.; Magin, T. E. *J. Chem. Phys.* **2013**, *138*, 044312.

[38] Valentini, P.; Schwartzentruber, T. E.; Bender, J. D.; Nompelis, I.; Candler, G. V. *Phys. Fluids* **2015**, *27*, 086102.

[39] Appleton, J. P.; Steinberg, M.; Liquornik, D. *J. Chem. Phys.* **1968**, *48*, 599–608.

[40] Cruden, B. A.; Prabhu, D.; Martinez, R.; Lee, H.; Bose, D.; Grinstead, J. H.; *Absolute Radiation Measurements in Venus and Mars Entry Conditions*; AIAA Paper AIAA-2010-4508; 2010.

[41] Mazaheri, A.; Gnoffo, P.; Johnston, C.; Kleb, B.; *Laura Users Manual*; NASA TM 2010-216836; 2010.

[42] Johnston, C.; Hollis, B.; Sutton, K. *J. Spacecr. Rockets* **2008**, *45*, 865–878.

[43] Johnston, C.; Hollis, B.; Sutton, K. *J. Spacecr. Rockets* **2008**, *45*, 879–890.

[44] Brandis, A.; Johnston, C.; Cruden, B. A.; Prabhu, D.; *Investigation of Nonequilibrium Radiation for Mars Entry*; AIAA Paper AIAA-2013-1055; 2013.

[45] Dean, A. J.; Davidson, D. F.; .Hanson, R. K. *J. Phys. Chem.* **1991**, *95*, 183–191.

[46] Thorne, L. R.; Branch, M. C.; Chandler, D. W.; Kee, R. J.; Miller, A. *Proceedings of the 21st Symposium (International) on Combustion, The Combustion Inst., Pittsburgh, PA* **1986**, 965–975.

[47] Prabhu, D. K. *personal communication.*

Table 1: Parameters for Analytic Representation of CO Dissociation Rate Coefficients

Source	A^a	n	T_{rxn} (K)	Temp. Range (K)	Comment
		CO+Ar			
Present work	3.910×10^{-9}	-	118712.6	7500-20000	2-p
	2.781×10^{-5}	-0.8514	128741.4	7500-20000	3-p, T_{rxn} fixed
Davies[11]	5.800×10^{-12}	0.5	92830	7000-9500	low-T
	2.620×10^{-13}	0.5	63820	9000-12000	high-T
	1.890×10^{12}	0.5	83550	7000-15000	all-T
Appleton *et al.*[12]	4.400×10^{-10}	-	98600	8000-15000	2-p
	2.800×10^{3}	-2.86	129000	8000-15000	3-p, T_{rxn} fixed
Mick*et al.*[13]	7.140×10^{3}	-3.1	129000	5500-9000	T_{rxn} fixed
Baulch[17]	1.461×10^{6}	-3.52	128700		T_{rxn} fixed
Park *et al.*[3]	3.819×10^{-5}	-1	129000		n,T_{rxn} fixed
Johnston and Brandis[18]	1.993×10^{-4}	-1	129000		n,T_{rxn} fixed
		CO+O			
Present Study	3.120×10^{-9}	-	108436.1	7500-20000	2-p
	1.733×10^{-1}	-1.7104	128741.4	7500-20000	3-p, T_{rxn} fixed
Appleton *et al.*[12]	6.860×10^{-9}	-	98025	8000-15000	2-p
Chackerian[15]	4.150×10^{-1}	-1.5	129000	6000-16000	T_{rxn} fixed
Hanson[16]	1.345×10^{-9}	-	83300		2-p
	1.330×10^{15}	-5.5	129000	5600-12000	3-p, T_{rxn} fixed
Baulch[17]	6.860×10^{-9}	-	98025		
Park *et al.*[3]	5.65×10^{-4}	-1	129000		n,T_{rxn} fixed
Johnston and Brandis[18]	1.993×10^{-3}	-1	129000		n,T_{rxn} fixed

^{a} units are cm^3 molec^{-1}s^{-1}.
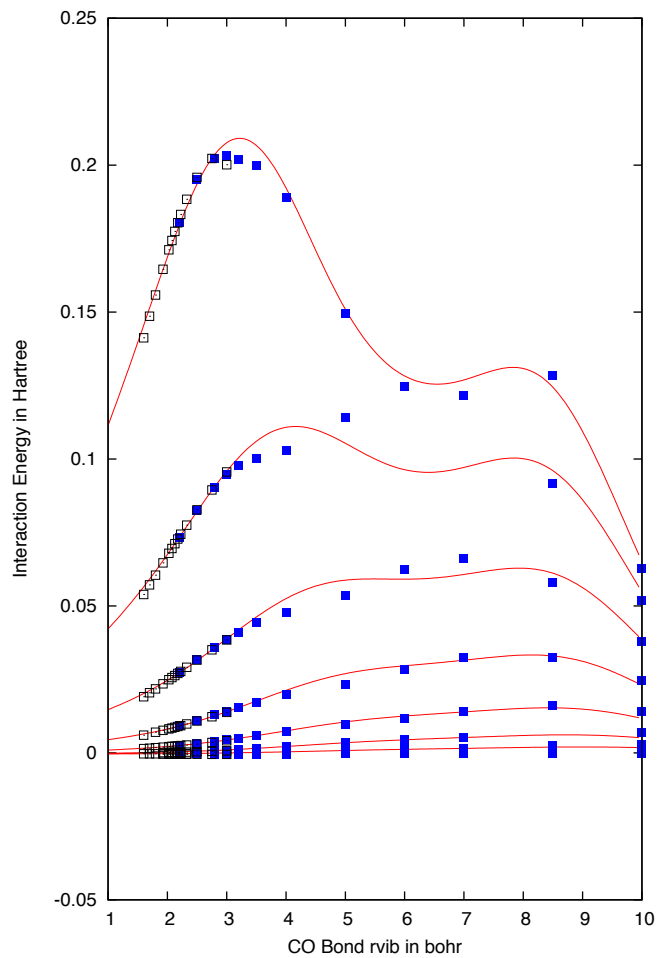
Figure 1: Cuts through CO+Ar PES with $\theta_a = 135°$. Black Open squares are V^{int} for CCSD(T) energies multiplied by 1.022, Blue filled squares are V^{int} for MRCI+Q energies, and the line is the analytic representation. The different cuts, from top to bottom, are for R_c =4, 4.5, 5, 5.5, 6, 6.5, 7, and 8 bohr.
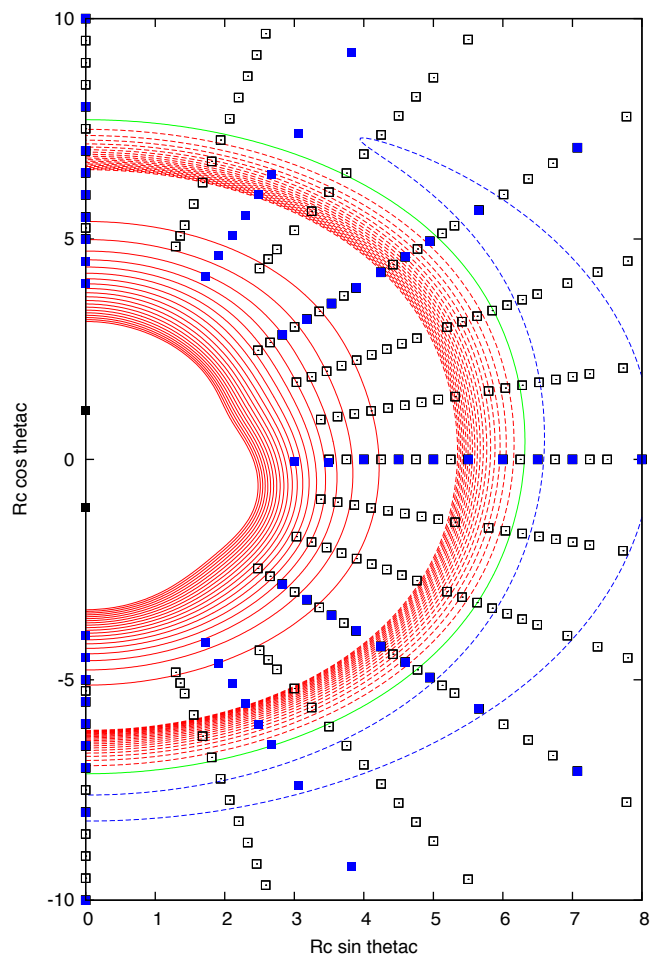
Figure 2: Contours for CO+Ar $r_{vib} = 2.2\,a_o$. Green is the zero contour, red are positive energy contours, and blue are negative energy contours. The solid curves are in steps of 0.05 E_h, and the dashed curves are in steps of 0.25 mE_h. The filled black squares show the C and O nuclear positions, with the O on top, and the blue filled squares show geometries where there are MRCI+Q calculations, and black squares show geometries where there are CCSD(T) calculations.
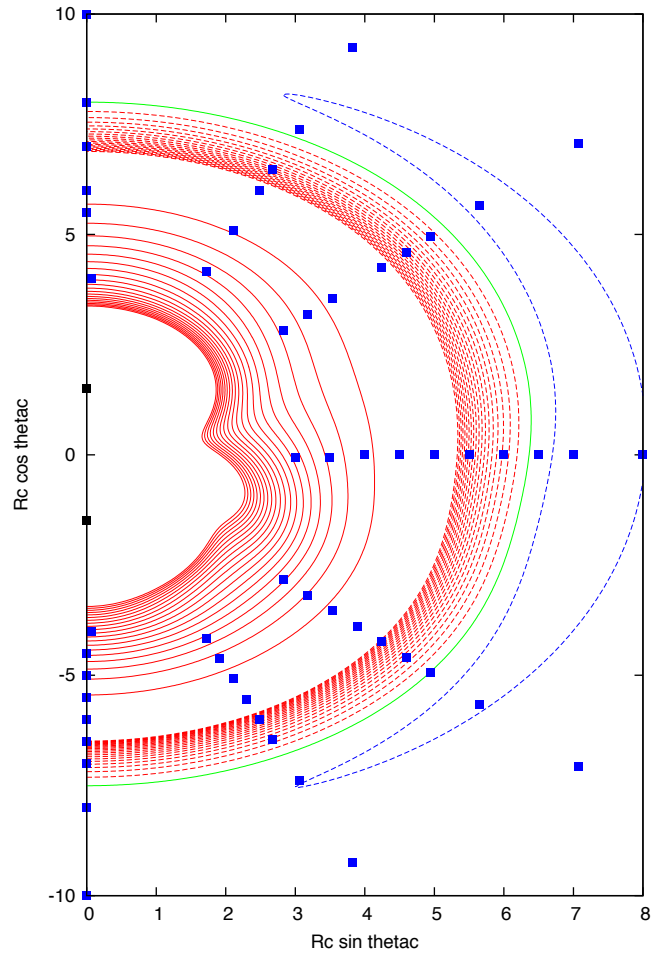
Figure 3: Same as Fig. 2, except $r_{vib} = 3\,a_o$.
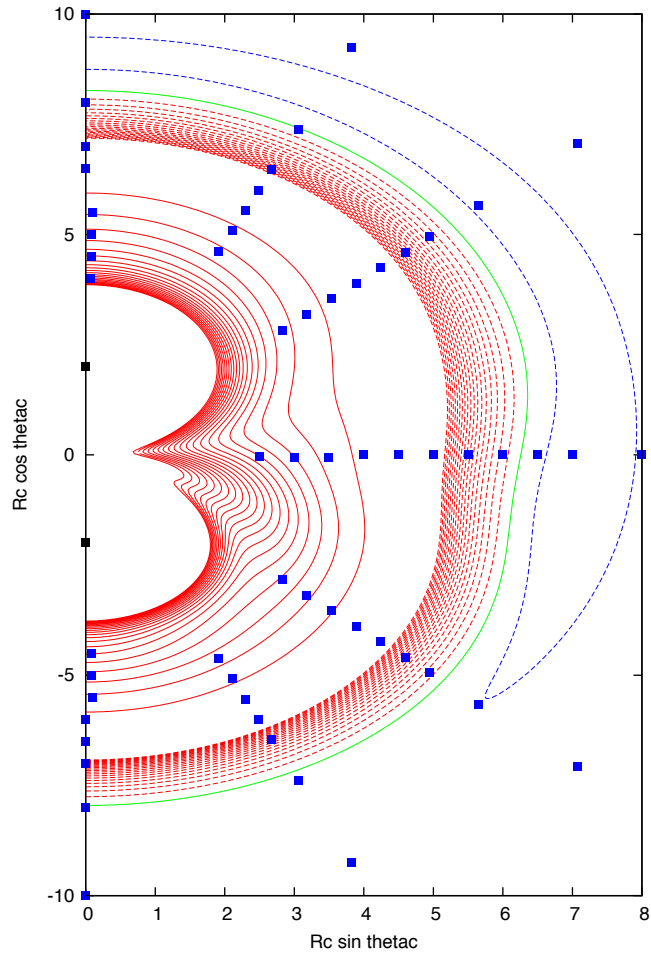
Figure 4: Same as Fig. 2, except $r_{vib} = 4\,a_o$.

31
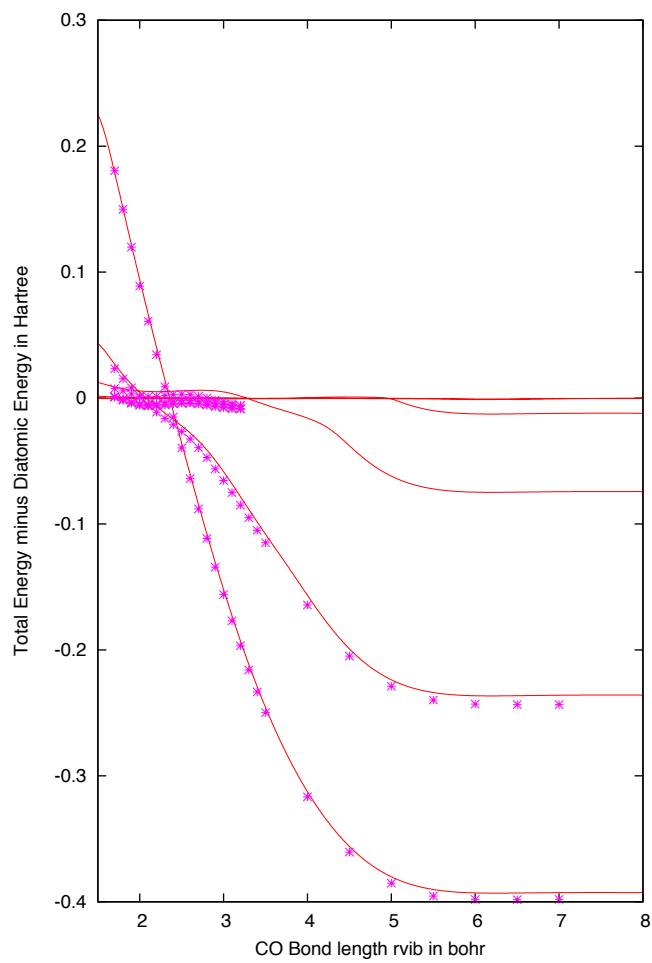
Figure 5: Cuts through OCO PES with OCO bond angle $120°$ for the $^3A'$ surface. Magenta stars are the Schmidt *et al.* energies, and the line is the analytic representation. The different cuts are for fixed CO bond lengths of 2, 3, 4, 5, 6, and 7 bohr.
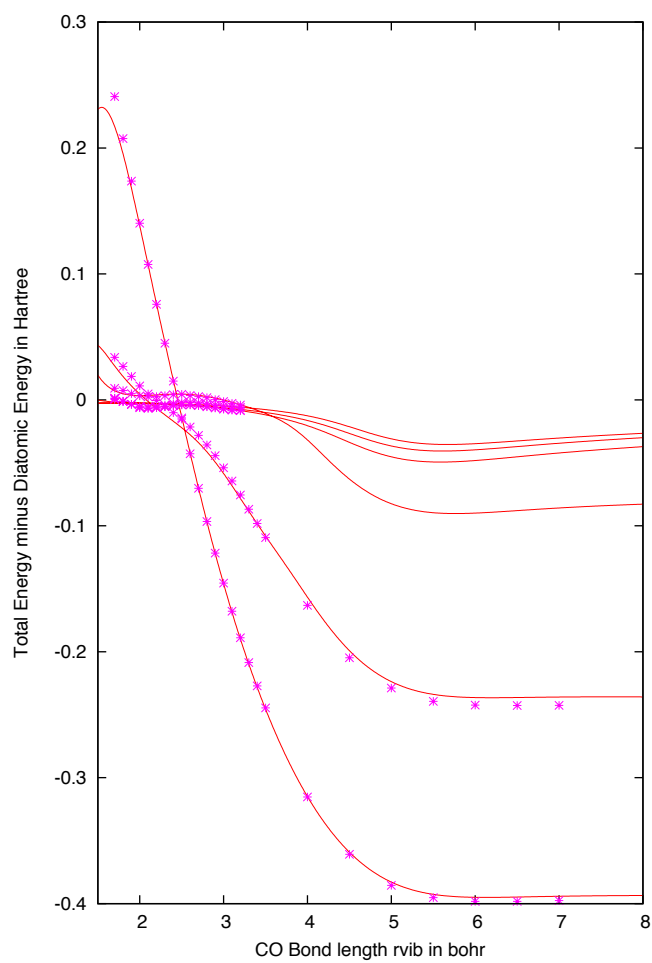
Figure 6: Same as Fig. 5 except lowest $^3A''$ surface.
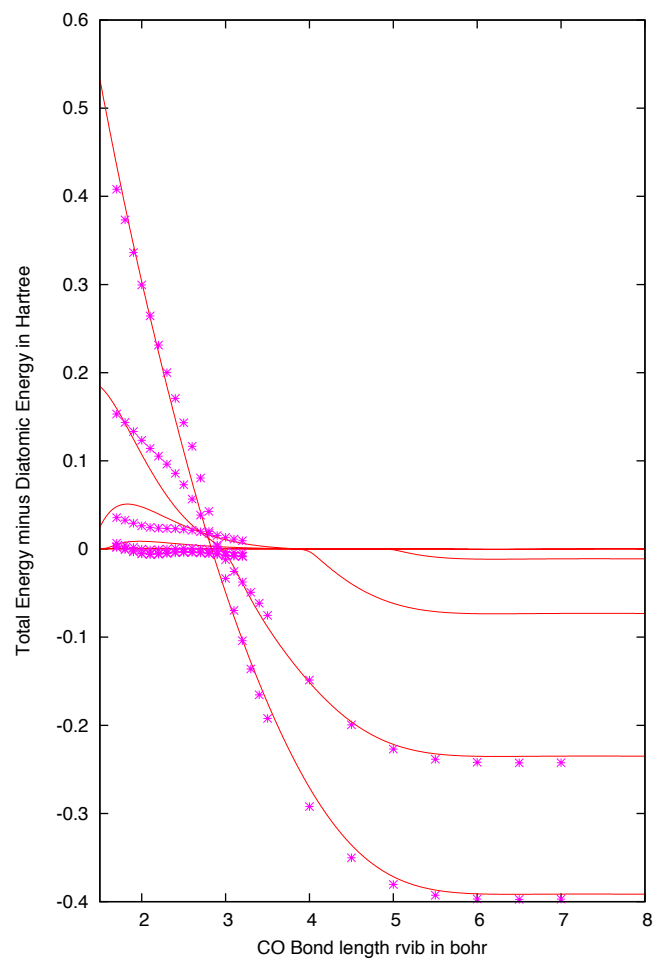
Figure 7: Same as Fig. 5 except second $^3A''$ surface.
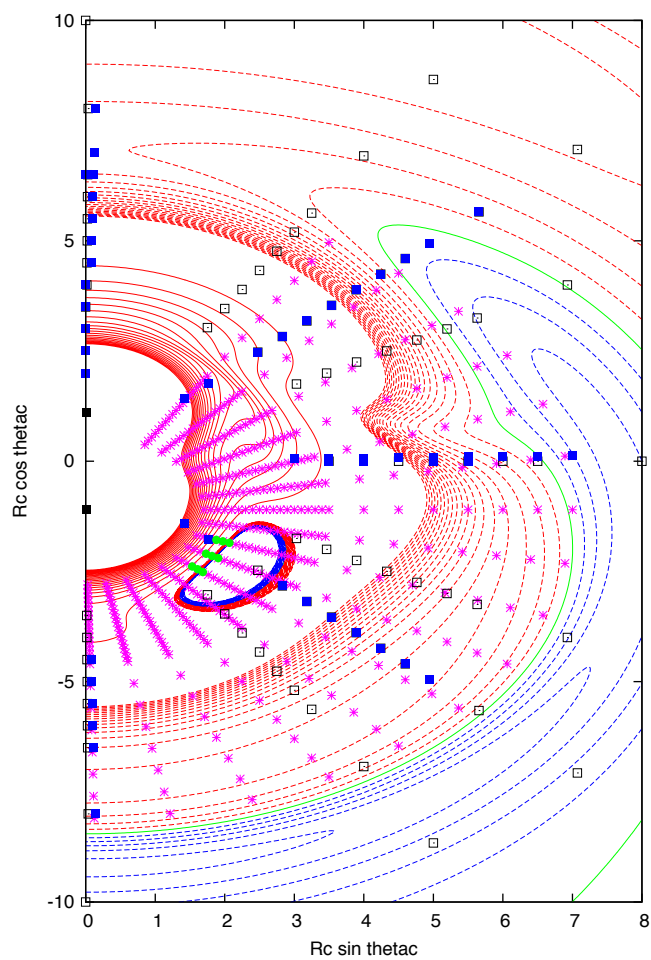
Figure 8: Same as Fig. 2 except $^3A'$ surface of CO+O: recall $r_{vib} = 2.2\,a_o$. The magenta stars show the geometries of the Schmidt *et al.* data, and the green filled squares show the geometries of the TZ CCSD(T) data.
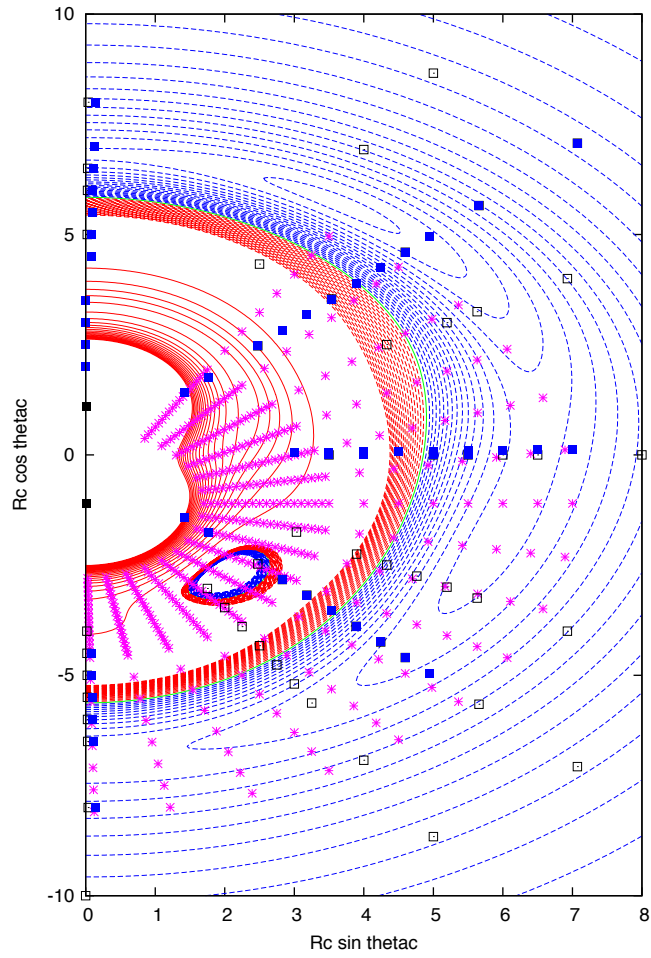
Figure 9: Same as Fig. 2 except lowest $^3A''$ surface of CO+O: $r_{vib} = 2.2\,a_o$. The magenta stars show the geometries of the Schmidt *et al.* data.
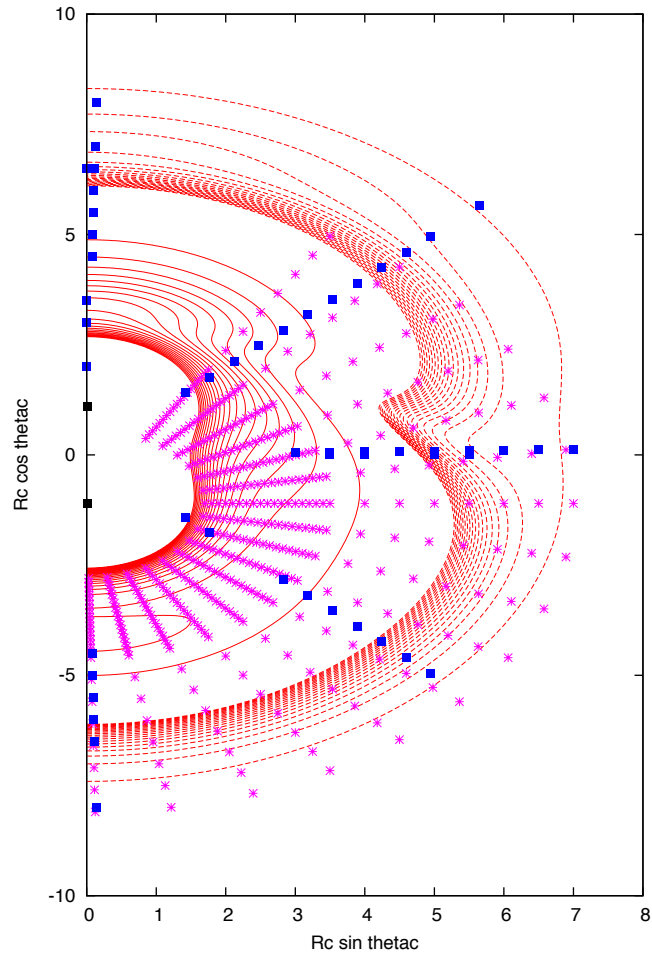
Figure 10: Same as Fig. 2 except excited $^3A''$ surface of CO+O: recall $r_{vib} = 2.2\,a_o$. The magenta stars show the geometries of the Schmidt *et al.* data.

37
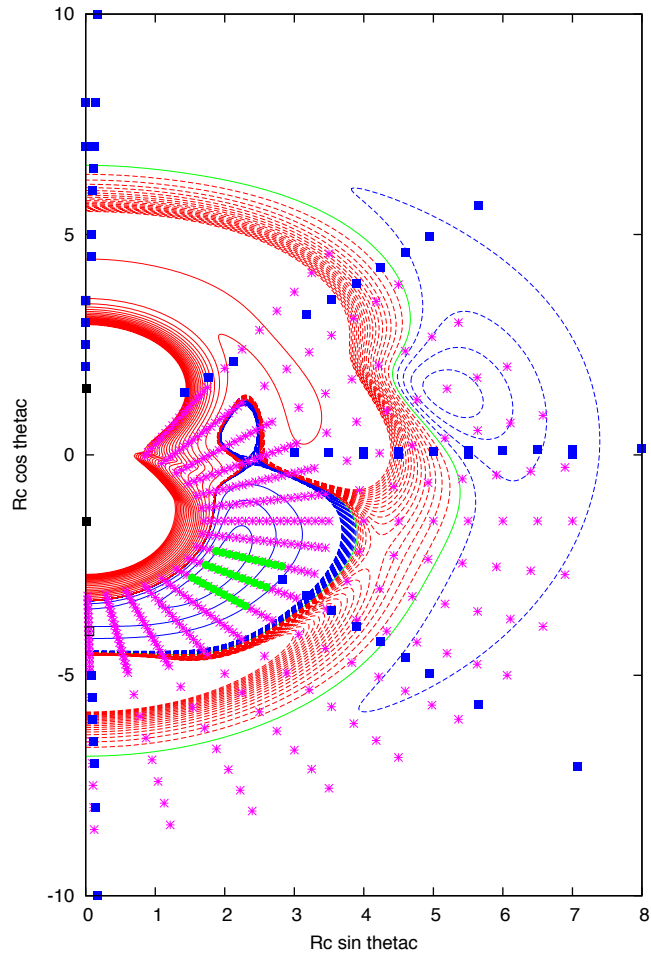
Figure 11: Same as Fig. 2 except $^3A'$ surface of CO+O and $r_{vib} = 3\,a_o$. The magenta stars show the geometries of the Schmidt *et al.* data.
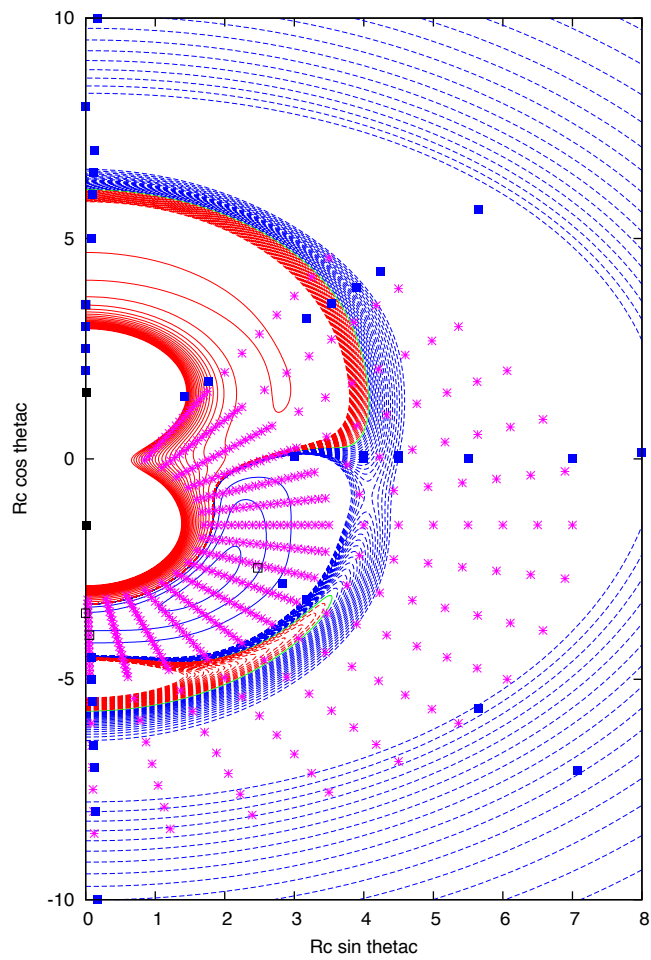
Figure 12: Same as Fig. 2 except lowest $^3A''$ surface of CO+O and $r_{vib} = 3\,a_o$. The magenta stars show the geometries of the Schmidt *et al.* data.

39
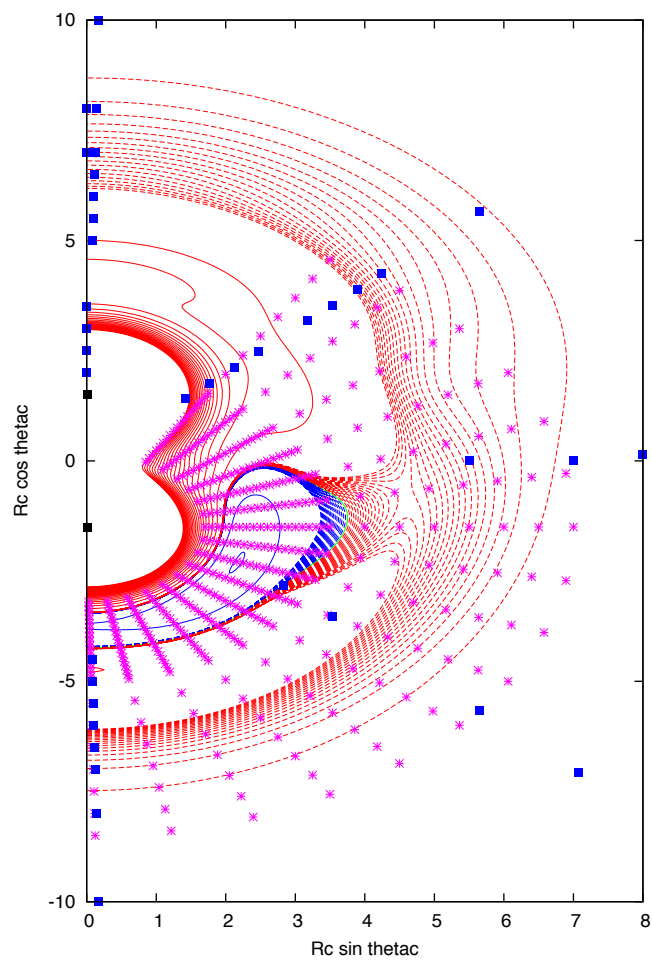
Figure 13: Same as Fig. 2 except excited $^3A''$ surface of CO+O and $r_{vib} = 3\,a_o$. The magenta stars show the geometries of the Schmidt *et al.* data.
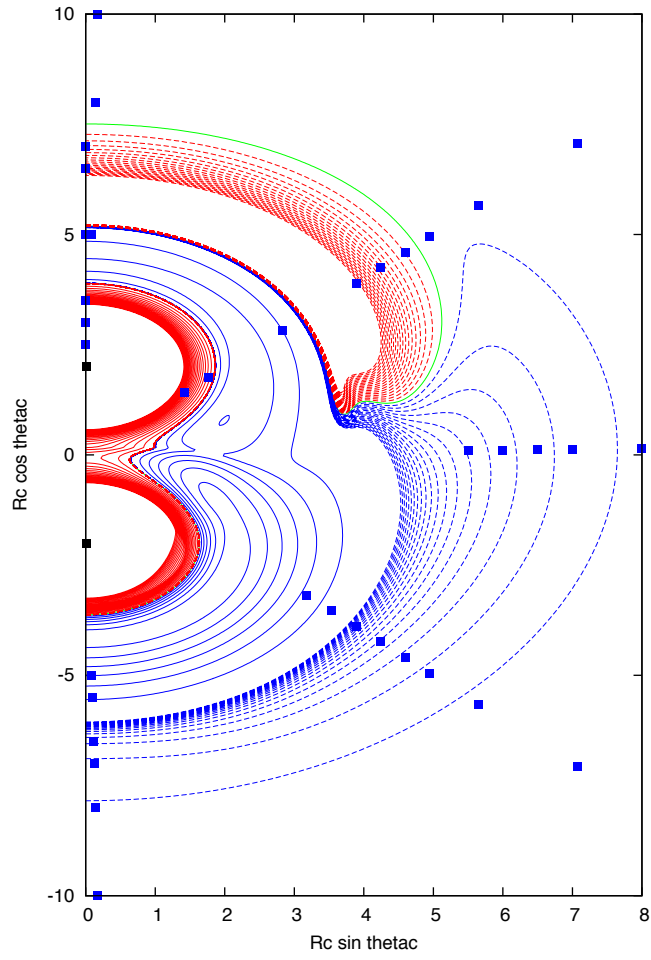
Figure 14: Same as Fig. 2 except $^3A'$ surface of CO+O and $r_{vib} = 4\,a_o$. The magenta stars show the geometries of the Schmidt *et al.* data.
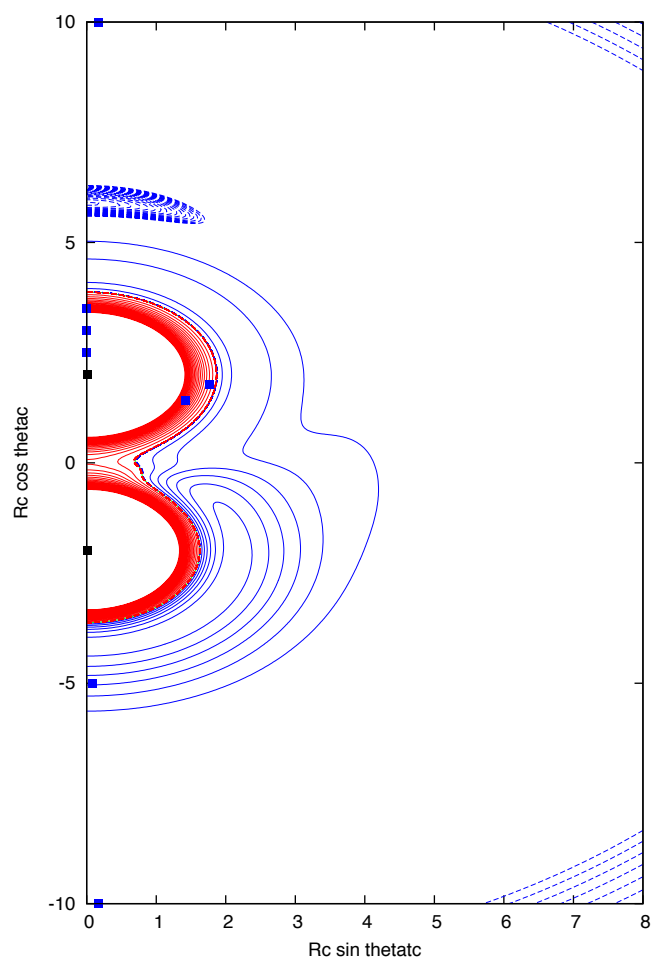
Figure 15: Same as Fig. 2 except lowest $^3A''$ surface of CO+O and $r_{vib} = 4\,a_o$.
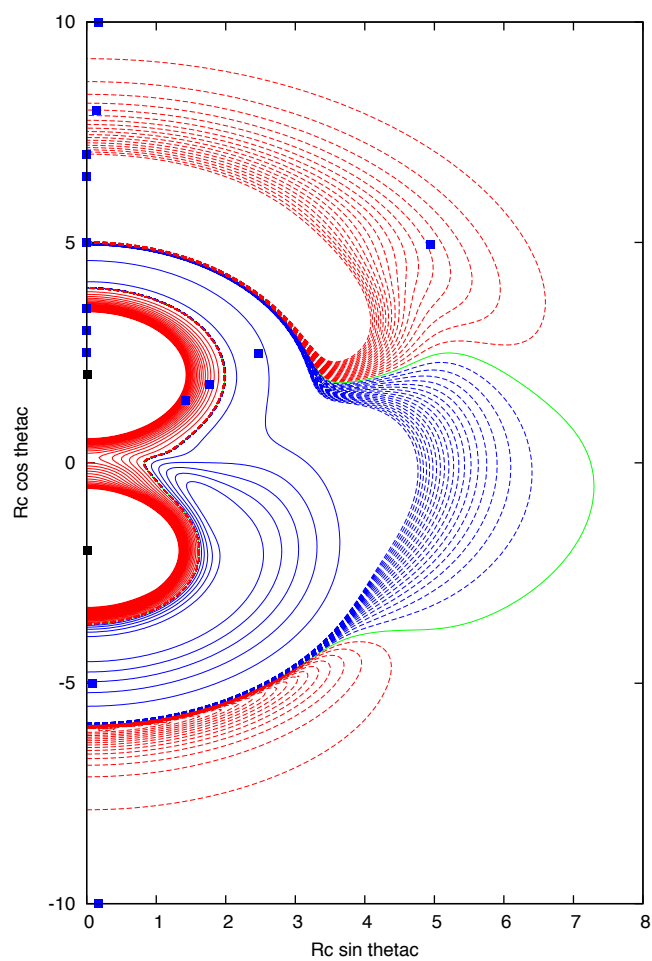
Figure 16: Same as Fig. 2 except second $^3A''$ surface of CO+O and $r_{vib} = 4\,a_o$.
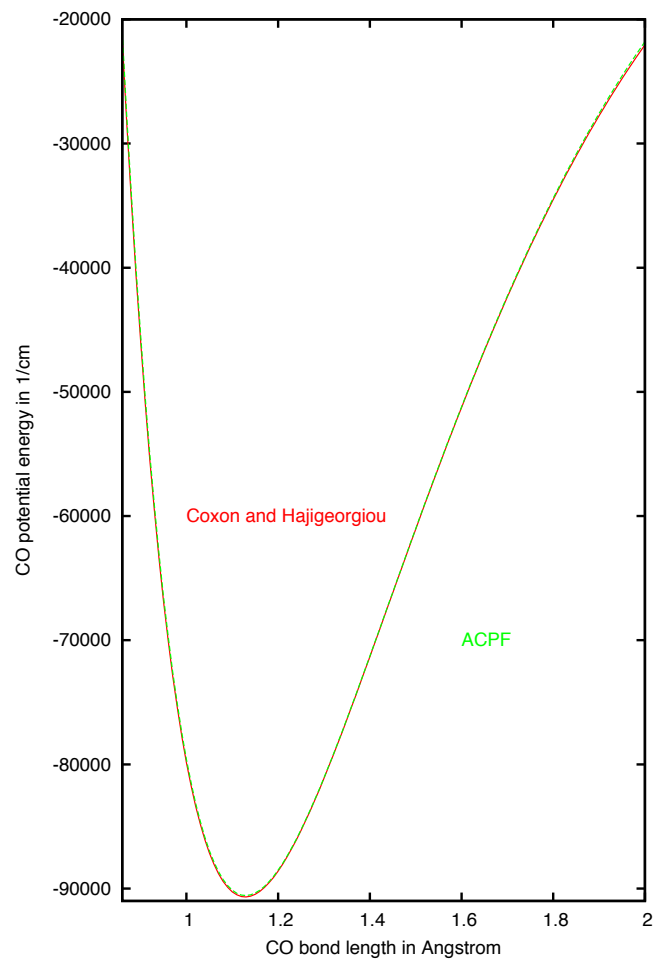
Figure 17: CO potential curve from fit to experimental data (red) and calculation (green).
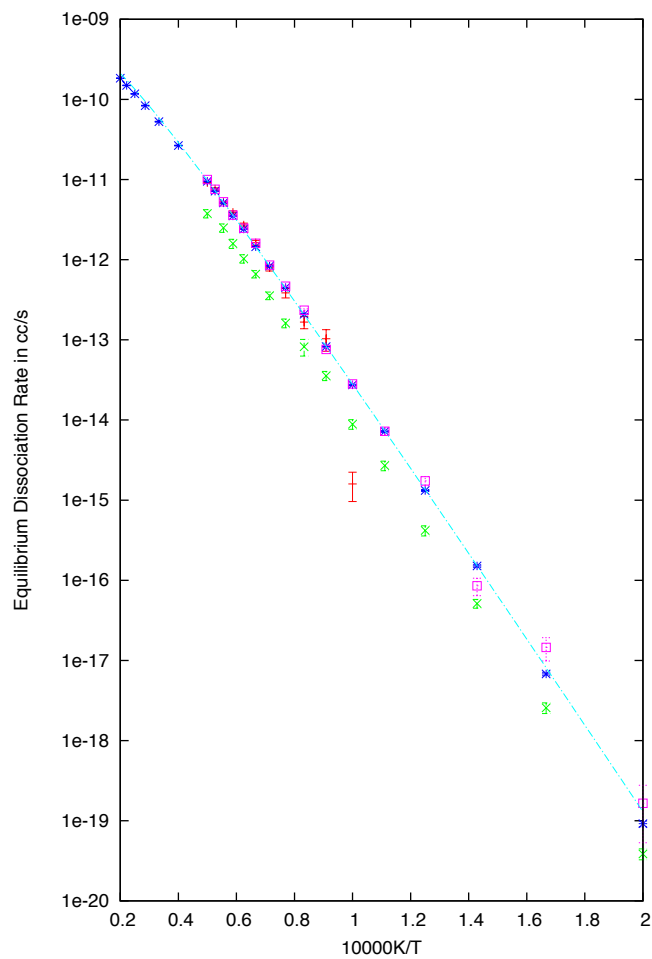
Figure 18: Computed dissociation rate coefficients for CO+Ar. Red samples from all CO ro-vibrational levels, green only from long lived quasi-bound levels, blue from levels within 0.1 E_h from the dissociation limit, and black from levels with 0.2 E_h from the dissociation limit. The cyan line shows the fit to the blue symbols.
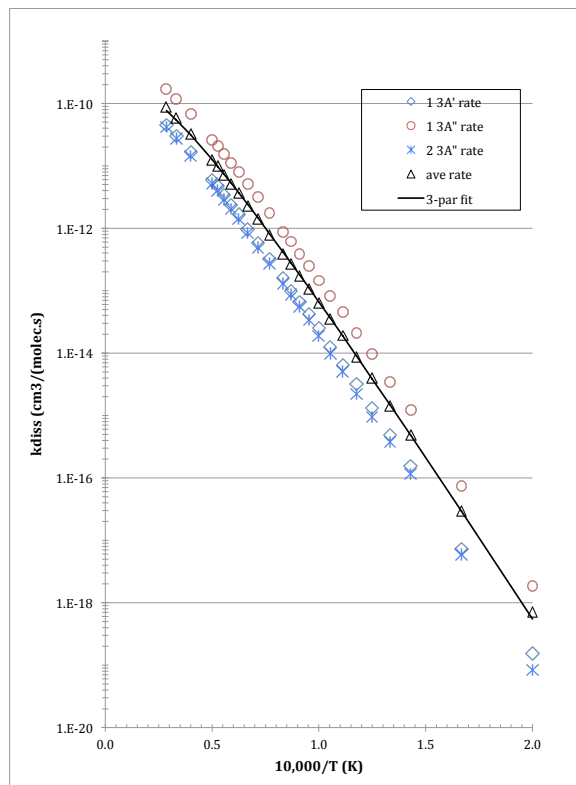
Figure 19: Computed dissociation rate coefficients for CO + O. CO ro-vibrational levels with energy greater than $D_0 - 0.1E_h$ are used in the calculations. Blue diamonds denote calculations for the $1^3A'$ PES, red circle denote calculations for the $1^3A"$ PES and blue Xs denote the $2^3A"$ PES. The total dissociation rate coefficient is the average of these three values and is denoted by the black triangles. The line represents the 3-parameter Arrhenius fit to the total rate coefficient.
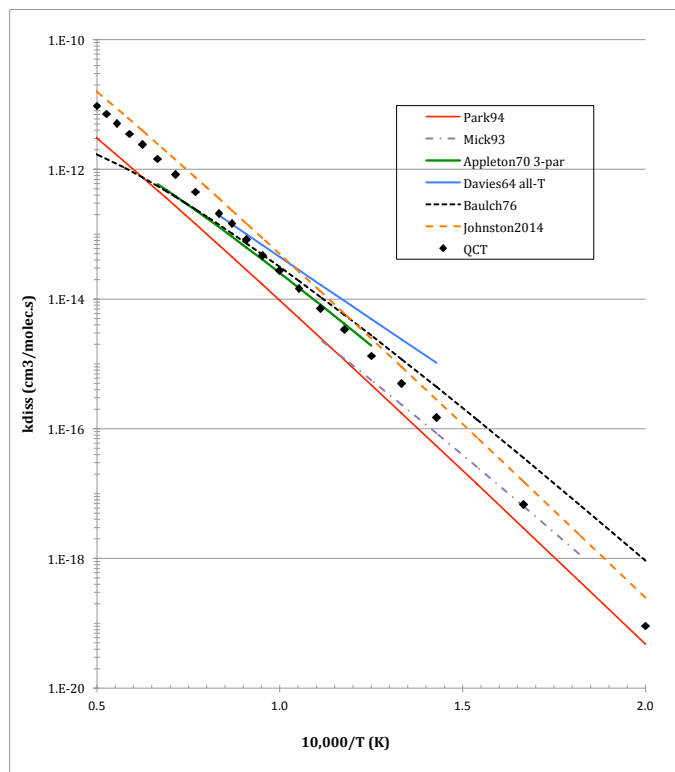
Figure 20: Dissociation rate coefficients for CO + Ar. Arrhenius fits to data from shock tube experiments by Davies[11] (blue line), Appleton et al.[12] (green line) and Mick et al.[13] and the review by Baulch et al.[17] (black dashed line). Also shown are the computed rate coefficients from the present study (black diamonds), the Arrhenius rate coefficient expressions used in the Park model[3] (red line) and the revised model of Johns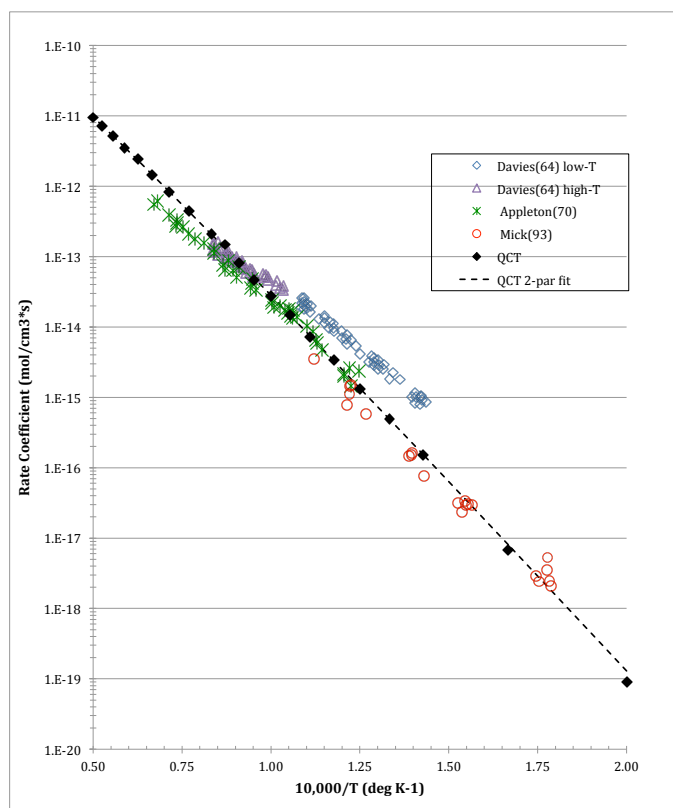ton and Brandis[18] (orange dashed line). CO ro-vibrational levels with energy greater than D_0-0.1E_h are used in the calculations.
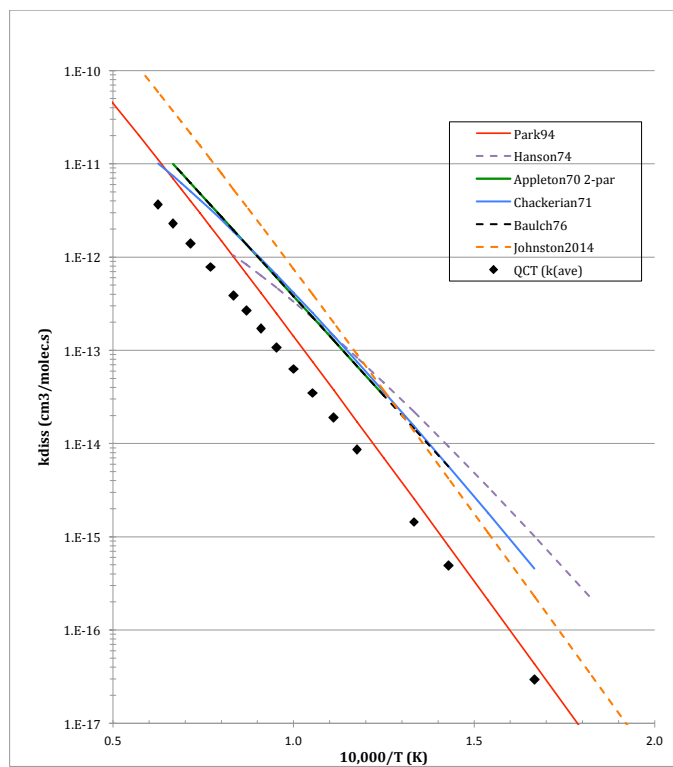
Figure 21: Dissociation rate coefficients for CO + O. Arrhenius fits to data from shock tube experiments by Appleton et al.[12] (green line), Chackerian[15] (blue line) and Hanson[16] and the review by Baulch et al.[17] (black dashed line). Also shown are the computed average rate coefficients from the present study (black diamonds), the Arrhenius rate coefficient expressions used in the Park model[3] (red line) and the revised model of Johnston and Brandis[18] (orange dashed line).

Figure 22: CO + Ar dissociation rate coefficient data from shock tube experiments. Points from Davies[11] and Appleton *et al.* [12] (X) read from figures and points from Mick *et al.* [13] (circles). Davies data divided into low-temperature (6000-9000 K) and high-temperature (9500-16,000 K) regimes (diamonds and triangles, respectively). Also shown are the QCT data points and 3-parameter Arrhenius fit from the present study.
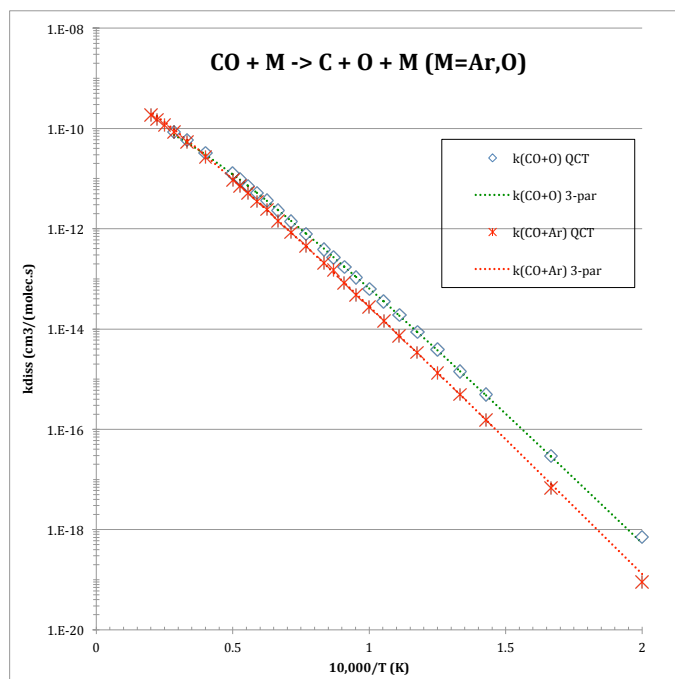
Figure 23: QCT Rate coefficients for CO dissociation due to collisions with Ar and O. Rovibrational levels greater than $D_0 - 0.1E_h$ are used in the calculations. Data points shown for CO + Ar (red Xs) and CO + O (blue diamonds). Lines are 3-parameter Arrhenius fits to the rate coefficients for the temperature range 7500 K to 20,000 K.
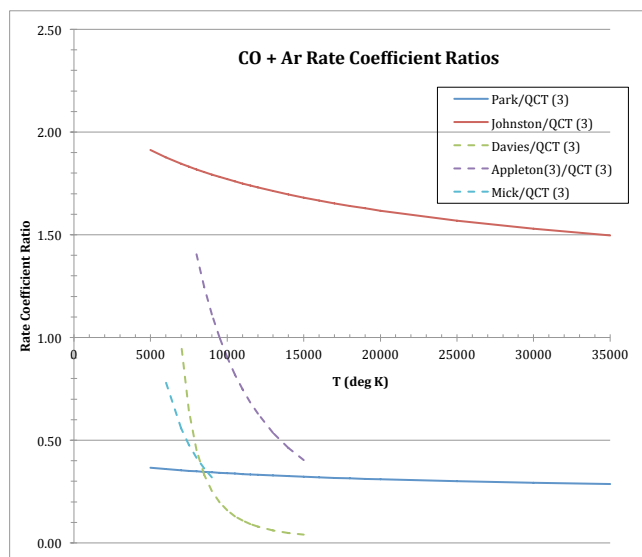
Figure 24: Ratios of published rate coefficients to QCT rate coefficients for CO dissociation due to collision with Ar. The horizontal axis is at a ratio of unity, which indicates complete agreement between present work and previous studies. The fits to the experimental data are shown over the temperature range of the experiments. The 3-parameter Arrhenius fit was used for the QCT values.
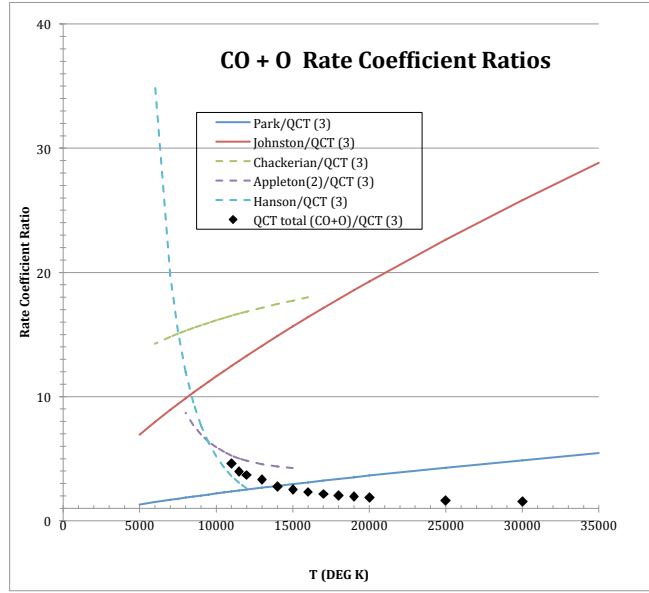
Figure 25: Ratios of published rate coefficients to QCT rate coefficients for CO dissociation due to collision with O atoms. The horizontal axis is at a ratio of unity, which indicates complete agreement between present work and previous studies. The fits to the experimental data are shown over the temperature range of the experiments. The 3-parameter Arrhenius fit was used for the QCT values. Also shown is the ratio of the total QCT rate coefficient for CO removal to the dissociation rate coefficient.
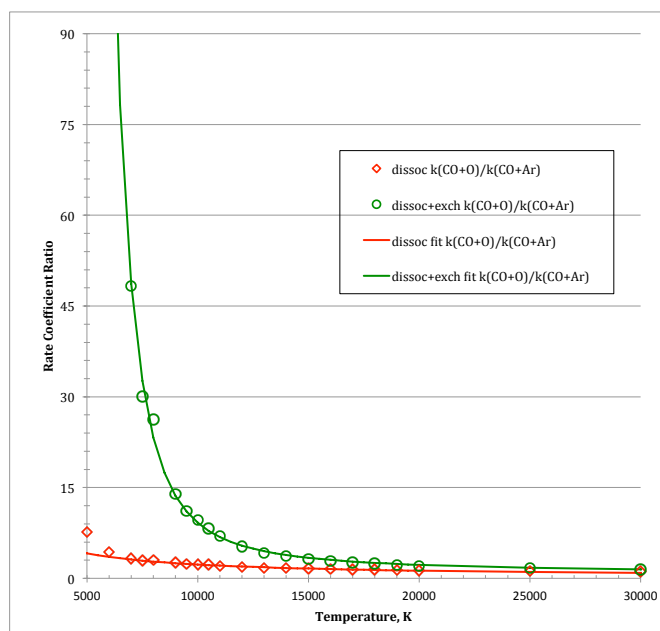
Figure 26: QCT rate coefficient ratios for CO removal due to collisions with O atoms and Ar. Red points only include dissociation: $k_{diss}^{\mathrm{CO+O}}/k_{diss}^{\mathrm{CO+Ar}}$ and green points are for dissociation plus exchange: $(k_{diss}^{\mathrm{CO+O}} + k_{exch}^{\mathrm{CO+O}})/k_{diss}^{\mathrm{CO+Ar}}$. The lines are ratios computed from the Arrhenius fits to the QCT data as described in the text.
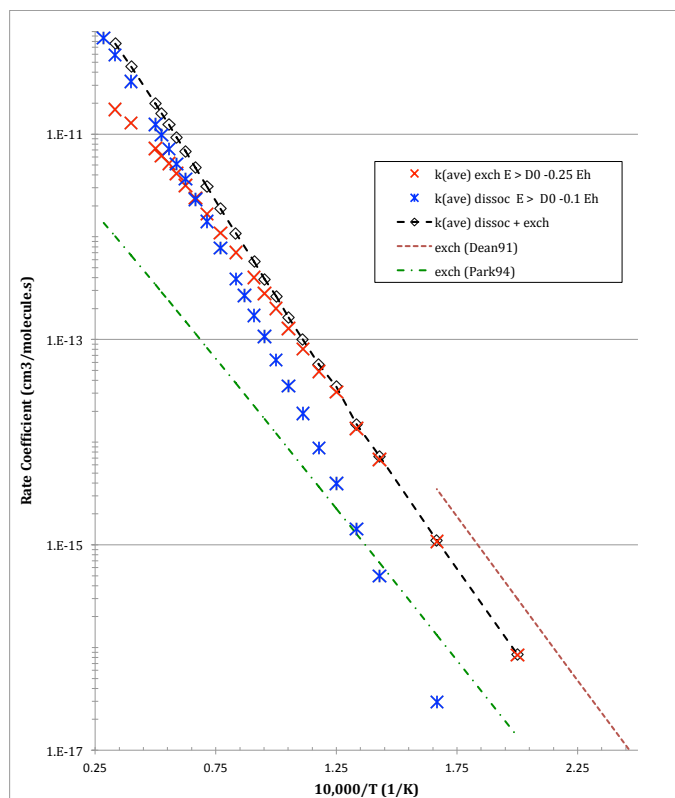
Figure 27: Rate Coefficients for $CO+O \rightarrow C+O_2$. Red symbols are for this reaction, blue symbols are for CO dissociation and the black dashed line is the sum of dissociation and exchange. Also shown are fitted rate coefficient expressions from Dean *et al.*[45] (salmon dashed line) and from the Park model [3] (green dot-dashed line). QCT rate coefficient are averaged over the data for the three PESs.